CHARACTERIZING DEPOSITS EMPLACED BY CRYOVOLCANIC PLUMES ON EUROPA

Dr. Lynnae C. Quick*

NASA Goddard Space Flight Center

Planetary Geology, Geophysics and Geochemistry Laboratory

8800 Greenbelt Road

Greenbelt, MD 20771

*Corresponding Author at: Lynnae.C.Quick@nasa.gov

Dr. Matthew M. Hedman

University of Idaho

Department of Physics

875 Perimeter Drive, MS 0903

Moscow, ID 83844

Abstract: In the absence of direct observations of Europa's particle plumes, deposits left behind during eruptive events would provide the best evidence for recent geological activity, and would serve as indicators of the best places to search for ongoing activity on the icy moon. Here, we model the morphological and spectral signatures of europan plume deposits, utilizing constraints from recent Hubble Space Telescope observations as model inputs. We consider deposits emplaced by plumes that are 1 km to 300 km tall, and find that in the time between the Galileo Mission and the arrival of the Europa Clipper spacecraft, plumes that are < 7 km tall are most likely to emplace deposits that could be detected by spacecraft cameras. Deposits emplaced by larger plumes could be detected by cameras operating at visible wavelengths provided that their average particle size is sufficiently large, their porosity is high, and/or they are salt-rich. Conversely, deposits emplaced by large plumes could be easily detected by near-IR imagers regardless of porosity, or individual particle size or composition. If low-albedo deposits flanking lineated features on Europa are indeed cryoclastic mantlings, they were likely emplaced by plumes that were less than 4 km tall, and deposition could be ongoing today. Comparisons of the sizes and albedos of these deposits between the Galileo and Europa Clipper missions could shed light on the size and frequency of cryovolcanic eruptions on Europa.

1. Introduction

The youthful and heavily fractured surface of Jupiter's moon Europa indicates that it has been geologically active in the relatively recent past. Multiple Hubble Space Telescope (HST) observations of large, water-vapor-dominated plumes suggest that the icy moon may currently be geologically active, with water vapor being actively vented into space [*Roth et al.*, 2014; *Sparks et al.*, 2016; 2017]. Additionally, a reanalysis of Galileo data suggests that several instruments aboard the spacecraft may have detected plume activity during low-altitude flybys of the moon [*Jia et al.*, 2018]. Meanwhile, *Fagents et al.* [2000] suggested that low-albedo deposits lying along lineaments and surrounding lenticulae on the icy moon could be ballistically-emplaced mantlings of cryoclastic material. Assuming that eruptive events were driven by volatiles such as CO, CO_2, SO_2 and NH_3, they constrained the dimensions of plumes that could have emplaced these deposits. Focusing solely on the particle component of Europan plumes, *Quick et al.* [2013] extended this analysis by constraining likely optical depth values and eruption lifetimes for these plumes. These authors assumed that the putative deposits imaged by the Galileo spacecraft were on the order of

55 1-10 m thick and consisted solely of particles with 0.5 μm radii. Similar to the results of *Fagents*
56 *et al.* [2000], they concluded that the dimensions of the dark deposits on Europa were consistent
57 with emplacement by plumes that were 2.5 - 26 km tall. Additionally, *Quick et al.* [2013] found
58 that plumes with optical depths ≥ 0.04 were most likely to be detected by spacecraft operating at
59 visible wavelengths. This optical depth value corresponded to $I/F \geq 0.07$, where I/F is a
60 standardized measure of the plume's reflectance, and particle column densities of 1.88×10^{-6}
61 kg/m^2 [*Quick et al.*, 2013].

62 Although recent HST observations suggest the presence of large vapor plumes [*Roth et al.*,
63 2014], previous searches for plumes in the Galileo dataset yielded null results, suggesting that
64 venting on Europa is not dominated by sizeable eruptions, and/or that eruptions may be sporadic
65 in nature [*Phillips et al.*, 2000]. Hence if large plumes are outliers, and most plumes on Europa are
66 indeed small in stature as has been suggested by image analysis [*Phillips et al.*, 2000; *Quick et al.*,
67 2010; *Bramson et al.,* 2011] and modeling [*Fagents et al.*, 2000; *Quick et al.*, 2013], it is possible
68 that active venting would have been missed by spacecraft cameras. Conversely, if plumes erupted
69 at a time when Galileo was not observing Europa's limb, or, if large plumes on Europa are similar
70 to Io's proposed "stealth plumes" [*Johnson et al.*, 1995], i.e., primarily composed of vapor-phase
71 volatiles, then cameras would have missed eruptions altogether. Moreover, the extent to which
72 thermal observations can be relied upon to reveal plume activity on Europa is unclear [*Rathbun*
73 *and Spencer*, 2018; 2019]. Thus, in the absence of direct, in-situ observations of active plumes,
74 the identification of fresh plume deposits may be the only tangible evidence of recent and/or
75 ongoing activity on Europa.

76 Searching for evidence of recent activity on Europa and determining the extent of material
77 exchange between the ice shell and ocean are key subgoals of NASA's Europa Clipper Mission

78 [*Europa Science Definition Team*, 2012; *Phillips and Pappalardo*, 2014; *Pappalardo et al.*, 2015;
79 *Turtle et al.*, 2016; 2019]. Given the large uncertainties surrounding the scale and frequency of
80 eruptions on Europa, constraining the dimensions and deposition rates of plume deposits may be
81 the best way to quantify current activity. Nevertheless, quantitative examinations of the
82 appearance of these deposits, and the potential for their detection by instruments on Europa Clipper
83 have been limited (but see *Southworth et al.* [2015]). While the presence of plume deposits may
84 be indicative of the presence of liquid water at shallow levels in the ice shell, plume deposit
85 dimensions could help to constrain rates of material exchange between the surface and subsurface
86 and provide a baseline from which the properties of the plumes that emplaced them could be
87 extrapolated. In addition, plume particle size distributions and deposition rates could be utilized to
88 predict the character of localized albedo changes caused by the emplacement of cryoclastic
89 particles on Europa's surface. Moreover, as is the case on Io where localized venting and the
90 subsequent deposition of pyroclastic deposits occurs contemporaneously with effusive eruptions
91 [*Geissler et al.*, 2004], cryoclastic particle deposition on Europa could occur within the same
92 timespan that cryolava is extruded onto the surface. Further, owing to their minimum exposure to
93 Europa's severe radiation environment, fresh plume deposits may contain and preserve organic
94 compounds (e.g., see *Nordheim et al.*, [2018]). The characterization of candidate plume deposits
95 is therefore a crucial step in gauging both the rates of occurrence, and probable locations of,
96 cryovolcanic activity on Europa. Their potential to contain biomarkers also makes their
97 identification a critical step in constraining Europa's habitability and astrobiological potential.

98 Here we employ the properties of candidate Europan plumes, gathered from observational
99 data and modeling, to characterize the dimensions, deposition rates, particle size distributions, and
100 spectral properties of their resulting deposits on Europa's surface. Europa's plumes may be

generated by exsolution of CO_2, SO_2, etc. in fractures propagating from the ocean to the surface [*Crawford and Stevenson*, 1988; *Fagents et al.*, 2000], or similar to Enceladus' plumes, by H_2O boiling at the surface of a water column exposed to the vacuum of space [cf. *Berg et al.* 2016]. It is unclear whether stress states in Europa's crust would allow fractures to extend from the surface directly to the ocean, especially if the icy crust is tens of km thick, or if the ice overlying the ocean is sufficiently ductile [*Crawford and Stevenson*, 1988; *Gaidos and Nimmo*, 2000; *Fagents*, 2003]. Hence we assume the latter case, in which plumes are generated by the boiling of a water column at 273 K. In this case, fractures that expose fluids to Europa's zero-pressure surface environment may be connected to fluid reservoirs that exist at shallow levels in the crust [c.f. *Gaidos and Nimmo*, 2000; *Fagents*, 2003; *Schmidt et al.*, 2011].

In Section 2, we introduce the dynamical and spectral models that were used to perform our analyses. We present our dynamical and spectral modeling results in Section 3 and discuss the implications of these results in Section 4. Finally, we conclude in Section 5 by placing constraints on the eruption rates that are necessary to emplace candidate plume deposits along lineaments on Europa. We also summarize the specifications of visible and near-IR imagers on the Europa Clipper spacecraft and comment on their ability to detect plume deposits on the icy moon. For reference, all variables that are utilized in our dynamical and spectral models are listed in Table 1.

Table 1. Plume and Deposit Parameters

Symbol	Parameter	Value	Unit
A	Deposit area	__	km^2
A_1	Brightness coefficient	__	
c_p	Specific Heat at Constant Pressure	__	J/K-kg
c_v	Specific Heat at Constant Volume	__	J/K-kg
D	Deposition rate	__	m/s
g	Acceleration due to gravity on Europa	1.31	m/s^2
H	Maximum plume height	1 - 300	km
H_P	Maximum height of individual plume particles	__	km
I/F	Plume Brightness	__	__
I/V	Ice to vapor mass ratio	__	__
k_B	Boltzmann's Constant	1.28×10^{-23}	J/K
L	Particle collision length	0.1	m
m	Mass of a water molecule	2.99×10^{-26}	kg
m_w	Molar mass of a water molecule	1.8×10^{-2}	kg/mol
m_p	Mass of individual plume particles as a function of size	__	kg
M	Total mass of plume particles	__	kg
M_P	Total mass of particles of a particular size		
M_v	Total mass of water vapor in the plumes	__	kg
n	Real index of refraction	__	__
n_f	Mass fraction of driving volatile	__	__
n_{gas}	Weight percent of driving volatile	0.1-100	%
N	Total number of particles in the plume	__	__
N_A	Avogadro's Number	6.022×10^{23}	kg/mol
N_p	Number of particles of a certain size in the plume	__	__
N_w	Total number of water molecules in the plume	__	__
r_c	Critical radius of plume particles	__	μm
R_g	Ideal gas constant	8.314	J/mol-K
R_p	Maximum range of plume particles	__	km
r_p	Plume particle radius	0.5 - 3	μm
r_{eff}	Effective average particle size in deposit		μm
S	Effective average scattering length in regolith		μm
$t_{deposit}$	Deposit accumulation time	__	hour; day; year
t_R	Particle residence time	__	s
T	Eruption temperature	240	K
T_D	Deposit thickness	__	m
T_{total}	Total deposit thickness per eruption	__	mm
$v = v_{gas}$	Maximum plume eruption velocity	__	m/s
v_p	Plume particle velocity	__	m/s
V_p	Volume of plume particles	__	m^3
α	Absorption Coefficient		μm^{-1}
β	Condensation coefficient	0.2	__
γ	Ratio of specific heats of water vapor (c_p/c_v)	1.334	__
θ	Particle eruption angle	45	°
κ	Molecular weight of water vapor	1.8×10^{-2}	kg/mol
κ_r	Imaginary index of refraction		
λ	Wavelength of light	1-2.5	μm
ρ_{gas}	Density of water vapor	4.85×10^{-3}	kg/m^3
ρ_p	Density of plume particles	920	kg/m^3
ϕ	Deposit porosity	0.5; 0.9	__

2. Materials and Methods

2.1 Dynamical Model

We utilize an analytical model, based on the work of *Quick et al.* [2013], to estimate the dimensions of deposits generated by a variety of plumes. While our model represents a simplification of the dynamics associated with plume particle deposition on Europa, such a simplified model allows us to explore the full parameter space as it relates to deposit dimensions and the sizes of plumes that may have emplaced them. As in *Quick et al.* [2013], we have assumed that eruptions are steady, i.e., the number of particles supplied to, and the particle discharge rate from, any plume as a function of time are both constant [*Parfitt and Wilson*, 2008]. We calculate the maximum travel distance of each plume particle assuming that particles are launched from eruptive sources regions at an angle of 45° from the horizontal and travel along ballistic trajectories. As suggested by HST observations, we assume that water vapor is the main volatile that drives eruptions [*Roth et al.*, 2014; *Sparks et al.*, 2016; 2017], and have utilized the methods of *Fagents et al.* [2000] and *Quick et al.* [2013] to constrain general plume particle eruption dynamics, assuming that plumes on Europa follow ballistic trajectories after ejection from the vent, a scenario which has been previously modeled for plumes on Enceladus [*Degruyter and Manga*, 2011].

We assume that plumes and their deposits consist of particles that range from 0.5 μm to 3μm in radius, consistent with the size range of plume particles on Enceladus and Io [*Cook et al.*, 1981; *Strom et al.*, 1981; *Collins et al.*, 1981; *Porco et al.*, 2006; *Spahn et al.*, 2006; *Kempf et al.*, 2008; *Postberg et al.*, 2008; *Hedman et al.*, 2009; *Kieffer et al.*, 2009; *Ingersoll and Ewald*, 2011]. Although plume particles may contain salts and other compounds (c.f. [*Postberg et al.*, 2008; 2011; 2018; *Hsu et al.*, 2015; *Porco et al.*, 2017]), for the sake of simplicity we assume that all particles are solely composed of water ice.

147 *2.1.1 Plume Parameters*

148 As eruptions are assumed to be vapor driven, the maximum velocity of the gas-particulate
149 mixture upon eruption may be expressed as:

150 $$v = v_{gas} = \sqrt{\frac{2n_f R_g T\gamma}{\kappa(\gamma-1)}} \quad (1)$$

151 [*Wilson and Head*, 1983; *Fagents et al.*, 2000] where n_f is the mass fraction of gas in the erupting
152 plume, R_g = 8.314 J/mol-K is the universal gas constant, and T is the gas temperature at the time
153 that the erupted material expands into Europa's zero-pressure surface environment. $\gamma = c_p/c_v$ =
154 1.334 and κ = 1.8 x 10^{-2} kg/mol represent the ratio of specific heats and the molecular weight,
155 respectively, of the volatile driving the eruption, which in this case is water vapor.

156 Equation (1) has been utilized in previous work to describe the velocities reached by grains
157 during explosive eruptions on both the moon and Europa [*Wilson and Head*, 1983; *Fagents et al.*,
158 2000]. In those cases, eruptions included volatile contents as low as 0.07 wt%, and 0.09 wt% (n_f =
159 7 x 10^{-4} and 9 x 10^{-4}), respectively, and plumes were 0.4 km to 1 km tall [*Fagents et al.*, 2000; L.
160 Wilson, personal communication]. Owing to their low volatile contents, these plumes would have
161 had very high solid to vapor mass ratios. In such particle-rich plumes, momentum is transferred
162 from the gas to the particles in order to keep the latter in motion. Particles will remain interspersed
163 in a dense column of gas near the vent, enabling efficient coupling between the gas and grains,
164 especially in cases when the solids to gas ratio is at least on the order of 10 [*Yeoh et al.*, 2015;
165 *Mahieux et al.*, 2019]. Icy particles in these plumes would therefore be in constant contact with
166 the driving gas [*Yeoh et al.*, 2015; *Berg et al.*, 2016]. Equation (1) describes the velocity of all of
167 the icy particles upon eruption as long as they remain coupled with the driving volatile (L. Wilson,
168 personal communication). Tables 2 and 3 illustrate that plumes ≤ 25 km tall will have low water
169 vapor content and will therefore have high enough ice to vapor mass ratio values (I/V) to be within

this limit (see Section 3). Thus, the velocity of icy particles, regardless of particle size, in plumes ≤ 25 km tall, is adequately described by (1).

Conversely, large plumes ($H \geq 50$ km) will have high vapor contents and relatively low *I/V* (Tables 2 & 3). Individual particles in plumes with $I/V \leq 1$ will interact more with the walls of the fissure than with other particles. As a consequence, their upward motion will be dependent upon how often they collide with the fissure walls before they can be reaccelerated by the driving gas [*Schmidt et al.*, 2008; *Yeoh et al.*, 2015]. Hence, while (1) is adequate to describe the motion of icy particles in small, particle-packed plumes, we must consider the velocity of particles as a function of size for large plumes with low *I/V*. The dynamics of icy particles in large Europan plumes may be similar to the dynamics of particles in Enceladus' plumes. We therefore apply the dynamical model of *Schmidt et al.* [2008] to obtain velocity distributions, as a function of particle size, for particles in plumes that are ≥ 50 km tall.

Schmidt et al. [2008] illustrated that plume particle speeds on Enceladus are affected by wall collisions and that particle acceleration is dependent upon gas density and particle size. Likewise, ionian plume dynamics are also dependent upon particle interactions with the driving gas [*Zhang et al.*, 2004; *Geissler and Goldstein*, 2006]. The average velocity $\langle v_p \rangle$ of plume particles as a function of particle radius, r_p, in large, low *I/V* plumes is:

$$\langle v_p(r_p) \rangle = {}^{v}\Big/\left(1 + \frac{r_p}{2r_c}\right) \tag{2}$$

[*Schmidt et al.*, 2008], where r_c, the critical radius, is expressed as:

$$r_c = \frac{\rho_{gas}}{\rho_p}\sqrt{\frac{8k_BT}{\pi m}}\left[1 + \frac{\pi}{8}(1-\beta)\right]\frac{L}{v} \tag{3}$$

[*Schmidt et al.*, 2008]. Here ρ_{gas} and ρ_p are the density of water vapor and icy particles, respectively, $k_B = 1.28 \times 10^{-23}$ J/K is Boltzmann's constant, and $m = 2.99 \times 10^{-26}$ kg is the mass of

192 one water molecule. β is a condensation coefficient, a quantity that represents the adsorption of
193 water molecules by ice grains [*Shaw et al.*, 1999; *Batista et al.*, 2005]. L is the collision length,
194 which represents the characteristic distance that particles are able to travel between collisions with
195 the walls of fractures that transport plume material to the surface. According to *Schmidt et al.*
196 [2008] particles with $r_p < r_c$ travel with $\langle v_p \rangle \sim v$, while particles with $r_p > r_c$ have wide velocity
197 distributions and their maximum velocity peaks at a speed $v_{max} < v$. We assume that all particles
198 are spherical and are solely composed of water ice [*Degruyter and Manga*, 2011; *Quick et al.*,
199 2013; *Hedman et al.*, 2018], so that $\rho_p = 920$ kg/m^3. As in *Schmidt et al.* [2008] we have assumed
200 that $\rho_{gas} = 4.85 \times 10^{-3}$ kg/m^3 is the density of water vapor.

201 Assuming ballistic trajectories for plume particles [*Fagents et al.*, 2000; *Quick et al.*, 2013],
202 the maximum height, H_p, that individual plume particles reach above the surface, regardless of
203 whether their motion is best described by (1) or (2), is:

204 $$H_p = \frac{v_p^2}{2g} \quad (4)$$

205 where g = 1.31 m/s^2 is the acceleration due to gravity on Europa. Assuming a particle eruption
206 angle $\theta = 45°$ from the horizontal, the range, R_p, which is the distance from the vent that plume
207 particles travel across the surface is:

208 $$R_p = 2H_p = \frac{v_p^2}{g} \quad (5)$$

209 The amount of time that particles spend in these plumes is represented by the particle residence
210 time, $t_R = 2v_p sin\theta/g$. Assuming a 45°particle eruption angle, t_R is calculated as:

211 $$t_R = \frac{2v_p sin\theta}{g} = \frac{v_p\sqrt{2}}{g} \quad (6)$$

212 Assuming that dark deposits along lineaments and surrounding lenticulae on Europa are
213 cryoclastic mantlings, *Fagents et al.* [2000] and *Quick et al.* [2013] suggested that plumes required

to emplace these deposits would extend, at most, 26 km above the surface. However, recent observations [*Roth et al.*, 2014; *Sparks et al.*, 2016; 2017] suggest that Europa's plumes have maximum heights between 50 and 300 km. In order to account for the broadest suite of plausible plume parameters, we consider eruptions where plume heights range from 1 to 300 km.

2.1.2 Plume Deposit Parameters

The volume of a plume deposit can be approximated as that of a thin disk. The area of the plume deposit, as a function of particle size, is:

$$A(r_p) = \pi R_p^2 \quad (7)$$

Consequently, plume deposit thickness as a function of particle size, $T_D(r_p)$, may be expressed by combining equations (3) and (4) from *Quick et al.* [2013]:

$$T_D(r_p) = \frac{4 r_p^3 N_p}{3 R_p^2 (1-\phi)} \quad (8)$$

Here N_p is the total number of particles of a given size in the plume, and hence in the resulting deposit, and ϕ represents deposit porosity.

The brightness of Enceladus' interstripe plains, which are believed to be covered by plume fallback, is consistent with that of freshly fallen snow [*Porco et al.*, 2006]. This implies that fresh plume deposits have a snow-like consistency. Freshly fallen snow has 90% pore space so that its porosity, ϕ = 0.9 [*Cuffey and Paterson*, 2010]. However, any subsequent coalescence and compression of plume particles, perhaps as a result of sintering or other processes, would generate a deposit with a porosity that is more consistent with dense snow, for which ϕ = 0.45 [*Quick et al.*, 2013]. We assume a slightly higher minimum porosity, ϕ = 0.5, for plume deposits in which particles have undergone a significant amount of compression and coalescence. We therefore assume that plume deposits have minimum porosities of 0.5, and maximum porosities of 0.9.

The masses of individual plume particles, which must be known in order to apply the model of *Schmidt et al.* [2008] to plumes with $H \geq 50$ km, is defined by $m_p = V_p \rho_p$, where $V_p = \frac{4}{3}\pi r_p^3$ is the volume of a particle. Assuming $\rho_p = 920$ kg/m^3, $m_p = 4.8 \times 10^{-16}$ kg, 3.9×10^{-15} kg, 3×10^{-14} kg, and 1×10^{-13} kg for icy particles with r_p = 0.5, 1, 2, and 3 μm, respectively. The total mass of plume particles, M, may be expressed as:

$$M = \sum N_p m_p \tag{9}$$

which, as will be shown in the next section, has been taken to be equal to the total mass of vapor in the plume, M_v, multiplied by the plume's ice to vapor ratio so that:

$$M = \sum N_p m_p = M_v * \left(\frac{I}{V}\right) = M_v * \left(\frac{1}{n_f} - 1\right) \tag{10}$$

N_p can be alternatively expressed as:

$$N_p = \frac{M_p}{m_p} \tag{11}$$

where M_p is the total mass of particles of the given size in the plume, which depends on the assumed particle size distribution. For the sake of simplicity, we will here assume that $M_p = M/4$ for all 4 discrete particle sizes, which yields values of N_p that are proportional to $1/r_p^3$. This, along with the non-uniform spacing of the particle sizes, is consistent with the observed particle size distributions observed in Enceladus' plume, which have a differential power-law index between 3 and 4 for micron-sized grains [*Ye et al.*, 2014].

In determining M_v for each plume in (10), we have used the only repeat observation of plumes on Europa, i.e., the 50 km tall plume described in *Sparks et al.* [2016; 2017], as a baseline from which to scale plume mass according to height. The reported column density of the 50 km plume is 1.8×10^{21} molecules/m^2, estimated $M_v = 5.4 \times 10^6$ kg, and the reported number of water molecules in the plume, N_w, is 1.8×10^{32} [*Sparks et al.*, 2017]. This implies an estimated plume

area equal to 1 x 10^{11} m^2. Scaling plume column density and area according to plume height for a 1 km tall plume returns a column density of 3.6 x 10^{19} molecules/m^2 and a plume area of 2 x 10^9 m^2. Multiplying these quantities together returns N_w = 7.2 x 10^{28} water molecules total in a 1 km tall plume. From here, M_v may be calculated according to the following relation:

$$M_v = \frac{N_w}{N_A} * m_w \quad (12)$$

where N_A = 6.022 x 10^{23} molecules/mol is Avogadro's number, and m_w = 1.8 x 10^{-2} kg/mol is the molar mass of one water molecule. Application of (12) returns M_v = 2.2 x 10^3 kg of water vapor for a 1 km tall plume. M_v for plumes with H = 10-300 km are listed in Table 3.

2.2 Spectral Model

The computed ranges and deposit thicknesses for various particle sizes can be translated into predictions for deposit spectra using light-scattering models that provide analytical expressions for the wavelength-dependent brightness of a surface [*Hapke,* 1981;1993; *Cuzzi and Estrada,* 1998; *Shkuratov et al.,* 1999]. These model spectra depend on both the composition and texture of the regolith, which are often quantified in terms of the product αS, where S is the mean scattering length of the photons within the surface regolith (also known as the regolith's "grain size"), and α is the absorption coefficient of the plume material, which is given by the expression $\alpha = 4\pi\kappa/\lambda$. Here κ_r is the imaginary part of the material's refractive index and λ is the wavelength of the radiation.

For this particular analysis, we will assume that the deposits are sufficiently thick so that the underlying material does not contribute to the spectrum. For the near-infrared wavelengths considered here, this corresponds to a deposit at least a few tens of microns thick, which is reasonable for the sources considered above. Finally, we assume that the scattering length S is equal to the average grain radius, r_{eff}, in the deposit, which is a function of the distance from the

vent. For the sake of simplicity, we assume that the deposit is composed of pure water ice. While plume deposits could include non-ice materials with distinctive spectral signatures, at present there are few constraints on the nature or concentration of such contaminants. Hence for this initial study we have chosen to focus on spectral trends associated with variations in the average grain size of icy particles in the plume deposits. Assuming a fixed composition allows us to utilize the optical constants determined by *Mastrapa et al.* [2009], specifically values of κ_r at each wavelength for crystalline ice at 120 K. The above assumptions will enable us to obtain a qualitative sense of the spectral trends in plume deposits. However, future work that considers a range of particle compositions and full particle size distributions will be needed to derive robust estimates of certain quantities such as the depths of specific bands.

In practice, we compute r_{eff} by first interpolating the above ranges and deposit thicknesses onto a regular grid of 100 particle sizes between 0.5 and 3 μm. Since these parameters are roughly power-law functions of the particle size, we perform these interpolations on the logarithms of the relevant parameters (i.e., we take the logarithm of the particle sizes and ranges, interpolate linearly between the computed values, and then take the exponential to recover the interpolated ranges). Then, for each radial distance from the vent, we compute the average particle size, r_{eff}, as the weighted average of the particle sizes in the deposit using the following formula:

$$r_{eff} = \frac{\sum r_p T_D(r_p)}{\sum T_D(r_p)} \quad (13)$$

where r_p are the individual particle sizes and T_D are the deposit thicknesses. Note that this sum only considers particles between 0.5 and 3μm, so the particle size distribution emerging from the vent is assumed to have hard cutoffs at 0.5 and 3μm.

The above estimates of α and r_{eff} =S can be used to compute the predicted spectra at each radius using the analytical models from *Cuzzi and Estrada* [1998], which uses a Hapke-based

304 formalism, or *Shkuratov et al.* [1999]. In practice, these two papers provide very different formulas
305 for albedo as a function of αS, and it is well known that the Hapke and Shkuratov scattering
306 theories can yield different estimates of the composition and effective scattering lengths required
307 to match a given spectrum [*Poulet et al.*, 2002]. In part, this is because *Cuzzi and Estrada* [1998]
308 compute the albedo of regolith, while *Shkuratov et al.*[1999] compute the albedo for a one-
309 dimensional model of a regolith surface. For this analysis, we prefer to use the *Shkuratov et al.*
310 [1999] model because it is explicitly designed for spectral analysis, while Hapke-based models are
311 better optimized for photometric studies. Hence for this analysis the expected value of the deposit's
312 brightness for a given αS is computed using equations 8-12 from *Shkuratov et al.* [1999]. For the
313 sake of simplicity, we assume here that the real part of the grains' refractive index is n = 1.3
314 (appropriate for ice-rich material) and zero porosity (note that including a finite porosity changes
315 the overall strength of spectral features, but not the trends with distance from the vent). In this
316 case, the relevant formula for the brightness can be written as:

317 $$A_1 = \frac{1+r_b^2-r_f^2}{2r_b} - \sqrt{\left(\frac{1+r_b^2-r_f^2}{2r_b}\right)^2 - 1} \qquad (14)$$

318 where the parameters r_b and r_f are given by the expressions:

319 $$r_b = R_b + \frac{1}{2}\frac{(1-R_e)(1-R_i)e^{-2\alpha S}}{1-R_i e^{-\alpha S}}$$

320 $$r_f = (R_e - R_b) + (1-R_e)(1-R_i)e^{-\alpha S} + \frac{1}{2}\frac{(1-R_e)(1-R_i)e^{-2\alpha S}}{1-R_i e^{-\alpha S}},$$

321 and the coefficients R_i, R_e and R_b are set by our choice of n:

322 $R_i \approx 1.04 - 1/n^2 \approx 0.45$

323 $R_e \approx (n\text{-}1)^2/(n+1)^2 + 0.05 \approx 0.067$

324 $R_b \approx (0.28\, n - 0.20)\, R_e \approx 0.011$

When using these formulae, it is important to understand that the parameter derived by *Shkuratov et al.* [1999] (here denoted A_1) is a ``brightness coefficient" of a one-dimensional model system viewed at low phase angles [*Shkuratov et al.* 1999]. The value of A_1 at any given wavelength should therefore not be mistaken for the Bond or single-scattering albedo of the surface [*Hedman et al.* 2013]. It is also important to note that the simplifications associated with the above model will fail around strong water-ice absorption bands, where the real index deviates strongly from 1.3 and the imaginary index is large. This model therefore does not provide reliable information about the shape of the deep water-ice absorption band around 3 microns. However, as prior work demonstrates that this model can reproduce the overall shape and depths of the 1.5 and 2.0 μm bands quite well for ice-rich surfaces [*Hedman et al.* 2013], this model is adequate for this initial study.

Once we have computed the model spectra of the plume deposits, we may calculate spectral parameters such as the 1.5 and 2.0 μm band depths. These band depths are simply the difference in brightness between the center of the band and the continuum on either side, normalized to the continuum brightness level. For the 1.5 μm band depth, we use the average A_1 between 1.5 and 1.55 μm to define the brightness in the center of the band, while the average A_i between 1.35-1.40 μm and 1.8-1.85 μm defines the continuum brightness level. For the 2.0 μm band depth, the average A_1 between 2.00 and 2.05 μm defines the brightness in the center of the band, while the average A_i between 1.80-1.85 μm and 2.20-2.25 μm defines the continuum brightness level. These simple estimates of the band depths are sufficient to illustrate trends in the deposit's spectral parameters with distance from the vent.

348 **Table 2.** Plume velocity (v) and height (H) as a function of wt% of water vapor (n_{gas}). Gas mass fraction, $n_f = n_{gas}/100$

n_{gas} (%)	v (m/s)	H (km)
0.1	30	0.34
0.2	42	0.67
0.3	52	1.0
0.4	60	1.3
0.5	67	1.7
0.6	73	2.0
0.7	79	2.3
0.8	84	2.7
0.9	89	3.0
1	94	3.4
2	133	6.7
3	163	10.1
4	188	13.4
5	210	16.8
6	230	20
7	249	23
8	266	27
9	282	30
10	298	34
15	364	50.3
20	421	67
25	471	84
30	515	101
35	557	117
40	595	134
45	631	151
50	665	168
55	698	185
60	729	201
65	759	218
70	787	235
75	815	252
80	842	268
85	868	285
90	893	302
95	917	319
100	941	335

Table 3. Cryovolcanic Plume Parameters: Plume Height (H), wt% (n_{gas}) and mass fraction (n_f) of water vapor, total mass of water vapor in the plume (M_v), total mass of icy particles in the plume (M), and ice to vapor ratios (I/V)

H (km)	n_{gas} (%)	n_f	M_v (kg)	M (kg)	I/V
1	0.3	0.003	2.2×10^3	7.2×10^5	332
10	3.0	0.030	2.2×10^5	6.9×10^6	32
25	7.4	0.074	1.4×10^6	1.7×10^7	12.5
50	15	0.15	*5.4×10^6	3.1×10^7	5.7
100	30	0.30	2.2×10^7	5×10^7	2.3
200	60	0.60	8.6×10^7	5.8×10^7	0.67
300	90	0.90	2×10^8	2×10^7	0.1

*Extracted from *Sparks et al.* [2017]

3. Results

3.1 Dynamical Model Results

3.1.1. Plumes with H = 1 km

According to (1) and (4), eruptions with a 0.3 wt% water vapor content will produce plumes that extend 1 km above Europa's surface. In this case, v_{gas} = 52 m/s, and the mass fraction of gas, $n_f = n_{gas}/100$ = 0.003 (Table 2). A 0.3 wt% water vapor content means that 99.7wt % or .997 mass fraction of a 1 km tall plume consists of icy particulates. In this case, I/V = .997/.003 = 332 (Table 3). Substituting $M_v = 2.2 \times 10^3$ kg and I/V = 332 into (10) returns $M = 7.2 \times 10^5$ kg for the total mass of ice in the plume. If we assume that the total mass of particles of each size is equal to ¼ the total mass of ice in the plume, then $M_p = ¼\ M = 1.8 \times 10^5$ kg as the total mass of particles of each size (i.e., r_p = 0.5 μm, 1 μm, etc.) in the plume, as well as in the resulting deposit. As mentioned in Section 2.1, icy particles in a 1 km tall plume will remain dispersed in a dense column of gas near the vent and will not be reaccelerated during the course of the eruption [*Yeoh et al.*, 2015]. Hence, we can assume that particles in these small plumes will travel at maximum speeds close to the gas speed (cf. *Fagents et al.* [2000]). In addition, the maximum particle deposition radius will be ~ 2 km from the vent (Table 4a).

Based on the duration of observations during which *Sparks et al.* [2017] identified plumes on Europa, those authors suggested that Europa's plumes have ~ 1 hour eruption timescales. Thus,

371 assuming continuous eruptions occur for at least an hour, deposits with 50% porosity (ϕ = 0.5)
372 would accumulate at rates of 8.6 x 10^{-9} m/s, while those with 90% porosity (ϕ = 0.9) would
373 accumulate at rates of 4.3 x 10^{-8} m/s (Table 4a). At these deposition rates, it would take almost 4
374 years to produce a 1 m thick deposit with 50% porosity; a similar deposit with 90% pore space
375 would take just under 9 months to form. In both cases the deposit would be spread over an area of
376 12.6 km^2 on the surface (Table 4a). The time for 10 m thick deposits to form can be determined
377 by multiplying the time it takes for 1 m deposits to accumulate by a factor of 10, so that a 10 m
378 thick deposit with 50% porosity would take 37 years to form, while a similar deposit with 90%
379 porosity would accumulate in just over 7 years (Table 4a). According to (6), particles in a 1 km
380 tall plume would have a residence time, t_R of 55 sec.

381 In order to determine the maximum distance that icy particles will travel across the surface,
382 we have considered 45° as the eruption angle at which plume particles will be ejected. In this way
383 we are able to obtain the maximum deposit radius for particles of a certain size. We assume that
384 all particles will be uniformly emplaced within a circle for which the outer radius is commensurate
385 with their maximum travel distance across the surface. However, it is likely that particles will be
386 ejected from the plume at a range of initial angles between 1° and 90° from the horizontal [*Fagents*
387 *et al.*, 2000; *Glaze and Baloga*, 2000; *Quick et al.*, 2013], so that there will be overlap between
388 deposits whose constituent particles are primarily of one size. In other words, plume deposits
389 consisting primarily of particles with r_p = 0.5 μm may overlap with deposits whose constituent
390 particles are mostly 2 or 3 μm in radius. It is therefore likely that deposits containing variable
391 particle sizes will build up on the surface. Assuming that each deposit contains particles of multiple
392 sizes, we find that a surface deposit emplaced during a single eruption of a 1 km tall plume could

393 be ~ 0.12 mm thick if the resulting deposit is 50% porous, and 0.62 mm thick if the deposit has
394 90% porosity (Table 4a).
395 *3.1.2. Plumes with H = 25 km*
396 These plumes would have 256 m/s gas speeds and would contain 7.4 wt% water vapor and 92.6
397 wt% icy particles, resulting in an I/V = 12.5 (Tables 2 & 3). Utilizing (9)-(12), and scaling plume
398 mass with height as described in Section 2.1, returns M_v = 1.4 x10^6, M = 1.7 x 10^7 kg and M_p = 4
399 x 10^6 kg. Here, the maximum particle deposition radius is 50 km (Table 4a). The resulting plume
400 deposits would be spread over a relatively wide area of Europa's surface, and particle deposition
401 rates would be 3 x 10^{-10} m/s for deposits with 50% porosity and 1.6 x 10^{-9} m/s for deposits with
402 90% pore space (Table 4a). Total deposits thicknesses, per eruption, would be 5 x 10^{-3} mm for
403 deposits with 50% pore space, and ~ 0.02 mm for deposits with 90% pore space. In the case of
404 deposits that are 90% porous, 1 m thick deposits will take less than 20 years to accumulate.
405 Conversely, 1 m thick deposits with 50% porosity would take almost 100 years to form (Table 4a).
406 *3.1.3. Plumes with H = 50 km*
407 Plumes that extend 50 km above Europa's surface would be composed of ~ 15 wt% water vapor
408 and 85 wt % icy particles. In this case v_{gas} = 362 m/s and I/V = 5.7 (Tables 2 - 3). *Sparks et al.*
409 [2017] report observations of a 50 km tall plume on Europa, with an estimated water vapor content
410 of 5.4 x 10^6 kg. Substituting M_v = 5.38 x10^6 kg and I/V = 5.7 into (10) returns M = 3.1 x 10^7 kg
411 and M_p = 7.7 x 10^6 kg. As previously mentioned, the dynamics of particles in plumes with $H \geq 50$
412 km may be described by equations (2) and (3). Employing (3) and assuming that plume expansion
413 begins at T = 240 K, ρ_{gas} = 4.85 x 10^{-3} kg/m^3, β = 0.2, and L = 0.1 m, commensurate with the
414 minimum collision length of plume particles on Enceladus, [*Schmidt et al.*, 2008], returns r_c = 1
415 μm. However, all particles peak at speeds less than v_{gas} (Table 4b), and only cryoclastic particles

416 with r_p = 0.5μm will reach the maximum particle deposition radius of 64 km (Fig. 1). The areal
417 extent of deposits emplaced by a 50 km tall plume would be quite broad and could cover an area
418 up to 1.3 x 10^4 km^2 (Fig. 2 & Table 4b). Particle deposition rates for hour-long eruptions range
419 from 4 x 10^{-10} – 6 x10^{-9} m/s, with the highest deposition rates occurring for particles with r_p = 3μm
420 (Table 4b). 1m thick deposits with 50% pore space could take as little as 6 years to accumulate if
421 primarily composed of particles with r_p = 3μm, while 1m thick deposits composed of particles
422 with r_p = 2μm could form in approximately 14 years. Conversely, 1 m thick deposits with 50%
423 pore space could take in excess of 40 years to accumulate if primarily composed of particles with
424 r_p = 1 μm, and 89 years to accumulate if primarily composed of particles with r_p = 0.5 μm (Table
425 4b). For all particle sizes considered, 1 m thick deposits with 90% pore space would take, at most,
426 20 years to form. Of note is that 1 m thick deposits, with ϕ = 0.9, that are primarily composed of
427 particles with r_p = 1-2 μm would take 9 and 3 years to accumulate, respectively, while it would
428 only take deposits composed of particles with r_p = 3 μm a year to form a 1 m thick layer on the
429 surface. If deposits consist of particles that vary in size so that particles with r_p ranging from 0.5
430 -3μm are present, total deposit thicknesses per eruption would be 0.03 mm and 0.16 mm for
431 deposits with ϕ = 0.5 and 0.9, respectively.

432 *3.1.4. Plumes with H = 200 km*

433 Plumes that extend 200 km above Europa's surface would be composed of ~ 60 wt% water vapor
434 and 40 wt% icy particles (Table 2). In this case, v_{gas} = 724 m/s, as previously reported [*Roth et al.*,
435 2014] and I/V = 0.67 (Table 3). We find that M_v would be 8.6 x 10^7 kg for plumes with H = 200
436 km. Substituting this value for M_v and I/V = 0.67 into (10) returns M = 5.8 x 10^7 kg, and M_p = 1.4
437 x 10^7 kg. Although according to (3) r_c = 0.5 μm, all particle velocities peak at values that are
438 substantially less than the gas speed. Particle deposition rates would be between 10^{-11} and 10^{-9} m/s

439 for deposits with 50% porosity, and between 10^{-10} and 10^{-8} m/s for deposits with 90% porosity.
440 (Table 4b). Total deposit thicknesses, per eruption, are 0.02 mm and 0.11 mm for deposits with ϕ
441 = 0.5 and 0.9, respectively. Our analysis shows that for the case of such large plumes, 1m thick
442 deposits with 50% pore space would take between 7.5 and 24 years to accumulate if primarily
443 composed of larger particles with r_p = 2-3 μm, and on the order of 100 years to accumulate if
444 composed of smaller particles with r_p = 0.5-1 μm (Table 4b). 1m thick deposits with 90% pore
445 space would take $\leq$ 24 years to accumulate if primarily composed of particles with $r_p \geq 1$ μm.
446 However if primarily composed of particles with r_p = 0.5 μm, 1m thick deposits could take as
447 much as 74 years to form. Particles ejected by plumes this size could be deposited as far as 180
448 km from their eruptive source regions (Fig. 1), and depending on particle size, the resulting
449 deposits could be spread over areas as large as 101,510 km^2 (Fig. 2 & Table 4b).
450 For plumes with $H \geq 50$ km, we find that only particles with submicron radii travel at
451 speeds identical to the gas speed (Fig. 3). This is similar to the case for plumes on Enceladus
452 [*Schmidt et al.*, 2008]. Utilizing equations (1)-(3), we find that for plumes with H = 50, 100, and
453 200 km, only particles with $r_p \leq 2 \times 10^{-3}$ μm, 1×10^{-3} μm, and 7×10^{-4} μm respectively, would
454 travel at speeds identical to the gas speed (Fig. 3). In the case of 300 km tall plumes, only particles
455 with $r_p \leq 6 \times 10^{-5}$ μm would travel at the gas speed (Fig. 3). Hence the larger the plume, the smaller
456 the particles must be in order to attain the gas speed. Figure 4 illustrates that in all of the plumes
457 considered in our study, the population of small particles (r_p = 0.5 μm) is larger than the population
458 of large particles (r_p = 3 μm) by 2-3 orders of magnitude. Additional details regarding particle
459 deposition for plumes for plumes with H = 10, 100 and 300 km can be found in Tables 4a-c.
460
461

Table 4a. Plume and Deposit Parameters for Small Plumes

	H = 1 km v = 51 m/s	H = 10 km v = 162 m/s	H = 25 km v = 256 m/s
$\mathbf{v_p}$ (m/s)	51	162	256
$\mathbf{H_p}$ (km)	1	10	25
$\mathbf{R_p}$ (km)	2	20	50
$\mathbf{t_R}$ (s)	55	175	276
A (km^2)	12.6	1257	7854
[a]$\boldsymbol{D_{\phi=50\%}}$ (m/s)	8.6 x 10^{-9}	8 x 10^{-10}	3 x 10^{-10}
$\boldsymbol{T_{D_{\phi=50\%}}}$(mm)	0.03	0.003	1.2 x 10^{-3}
$\boldsymbol{T_{total\,\phi=50\%}}$ per eruption	**0.12 mm**	**0.01 mm**	**0.005 mm**
[b]$\mathbf{t_{deposit}}$ = 1 m	3.7 yr	38 yr	98 yr
[c]$\mathbf{t_{deposit}}$ = 10 m	37 yr	383 yr	976 yr
[d]$\boldsymbol{D_{\phi=90\%}}$ (m/s)	4.3 x 10^{-8}	4.1 x 10^{-9}	1.6 x 10^{-9}
$\boldsymbol{T_{D_{\phi=90\%}}}$(mm)	0.15	0.015	5.8 x 10^{-3}
$\boldsymbol{T_{total\,\phi=90\%}}$ per eruption	**0.62 mm**	**0.06 mm**	**0.02 mm**
[e]$\mathbf{t_{deposit}}$ = 1 m	0.74 yr	7.7 yr	19.5 yr
[f]$\mathbf{t_{deposit}}$ = 10 m	7.4 yr	77 yr	195 yr

[a,d]Particle deposition rate assuming each individual eruption is continuous for 1 hour

[b,c]time to accumulate 1 m and 10 m thick deposits assuming individual eruptions last for one hour, when $\phi = 50\%$

[e,f]time to accumulate 1 m and 10 m thick deposits assuming individual eruptions last for one hour, when $\phi = 90\%$

Table 4b. Plume and Deposit Parameters for Large Plumes

	H = 50 km v = 362 m/s				H = 100 km v = 512 m/s				H = 200 km v = 724 m/s			
	r_p (μm)				r_p (μm)				r_p (μm)			
	0.5	1	2	3	0.5	1	2	3	0.5	1	2	3
$\mathbf{v_p}$ (m/s)	291	243	182	146	380	302	214	166	485	365	244	183
$\mathbf{H_p}$ (km)	32	22	13	8	55	35	17	10	90	51	23	13
$\mathbf{R_P}$(km)	64	45	25	16	110	70	35	21	180	102	45	26
$\mathbf{t_R}$ (s)	314	262	197	158	410	326	231	179	524	394	263	198
A (km^2)	13,043	6344	2029	837	38,078	15,200	3843	1384	101,510	32,466	6483	2062
[a]$\boldsymbol{D_{\phi=50\%}}$ (m/s)	4x10^{-10}	7 x10^{-10}	2 x10^{-9}	6 x 10^{-9}	2 x10^{-10}	5 x10^{-10}	2 x10^{-9}	5 x10^{-9}	9 x 10^{-11}	3 x 10^{-10}	1 x10^{-9}	4 x10^{-9}
$\boldsymbol{T_{D_{\phi=50\%}}}$**(mm)**	1 x 10^{-3}	3 x 10^{-3}	0.01	0.02	7 x 10^{-4}	2 x 10^{-3}	7 x 10^{-3}	0.02	3 x 10^{-4}	1 x 10^{-3}	5 x 10^{-3}	0.02
$\boldsymbol{T_{total\,\phi=50\%}}$ per eruption	**0.03 mm**				**0.03 mm**				**0.02 mm**			
[b]$\mathbf{t_{deposit}}$ = 1 m	89 yr	43 yr	14 yr	6 yr	161 yr	64 yr	16 yr	6 yr	369 yr	118 yr	24 yr	7.5 yr
[c]$\mathbf{t_{deposit}}$ = 10 m	891 yr	433 yr	139 yr	57 yr	1614 yr	644 yr	163 yr	59 yr	3689 yr	1180 yr	236 yr	75 yr
[d]$\boldsymbol{D_{\phi=90\%}}$ (m/s)	2 x10^{-9}	4 x10^{-9}	1 x 10^{-8}	3 x 10^{-8}	9.8 x10^{-10}	2 x10^{-9}	9.7 x10^{-9}	3 x 10^{-8}	4 x 10^{-10}	1 x 10^{-9}	7 x10^{-9}	2 x10^{-8}
$\boldsymbol{T_{D_{\phi=90\%}}}$**(mm)**	6 x 10^{-3}	0.01	0.04	0.1	4 x 10^{-3}	9 x 10^{-3}	0.03	0.1	2 x 10^{-3}	5 x 10^{-3}	0.02	0.08
$\boldsymbol{T_{total\,\phi=90\%}}$ per eruption	**0.16 mm**				**0.14 mm**				**0.11 mm**			
[e]$\mathbf{t_{deposit}}$ = 1 m	18 yr	9 yr	3 yr	1 yr	32 yr	13 yr	3 yr	1 yr	74 yr	24 yr	5 yr	1.5 yr
[f]$\mathbf{t_{deposit}}$ = 10 m	178 yr	87 yr	28 yr	11 yr	323 yr	129 yr	33 yr	12 yr	738 yr	236 yr	47 yr	15 yr

[a,d]Particle deposition rate assuming each individual eruption is continuous for 1 hour

[b,c]time to accumulate 1 m and 10 m thick deposits assuming individual eruptions last for one hour, when $\phi = 50\%$

[e,f]time to accumulate 1 m and 10 m thick deposits assuming individual eruptions last for one hour, when $\phi = 90\%$

Table 4c. Plume and Deposit Parameters for Plumes with $H = 300$ km

	$H = 300$ km, $v = 887$ m/s, r_p (μm)			
	0.5	1	2	3
$\mathbf{v_p}$ (m/s)	553	402	260	192
$\mathbf{H_p}$ (km)	117	62	26	14
$\mathbf{R_P}$(km)	234	123	52	28
$\mathbf{t_R}$ (s)	597	434	281	207
A (km^2)	171,520	47, 852	8366	2494
[a]$\boldsymbol{D_{\phi=50\%}}$ (m/s)	1.7×10^{-11}	6×10^{-11}	4×10^{-10}	1×10^{-9}
$\boldsymbol{T_{D_{\phi=50\%}}}$**(mm)**	6×10^{-5}	2×10^{-4}	1×10^{-3}	4×10^{-3}
$\boldsymbol{T_{total_{\phi=50\%}}}$ per eruption	**5.86×10^{-3} mm**			
[b]$\mathbf{t_{deposit}}$ = 1 m	1825 yr	509 yr	89 yr	27 yr
[c]$\mathbf{t_{deposit}}$ = 10 m	18,250 yr	5092 yr	890 yr	265 yr
[d]$\boldsymbol{D_{\phi=90\%}}$ (m/s)	9×10^{-11}	3×10^{-10}	2×10^{-9}	6×10^{-9}
$\boldsymbol{T_{D_{\phi=90\%}}}$**(mm)**	3×10^{-4}	1×10^{-3}	6×10^{-3}	2×10^{-2}
$\boldsymbol{T_{total_{\phi=90\%}}}$ per eruption	**0.03 mm**			
[e]$\mathbf{t_{deposit}}$ = 1 m	365 yr	102 yr	18 yr	5 yr
[f]$\mathbf{t_{deposit}}$ = 10 m	3650 yr	1018 yr	178 yr	53 yr

[a,d]Particle deposition rate assuming each individual eruption is continuous for 1 hour

[b,c]time to accumulate 1 m and 10 m thick deposits assuming individual eruptions last for one hour, when $\phi = 50\%$

[e,f]time to accumulate 1 m and 10 m thick deposits assuming individual eruptions last for one hour, when $\phi = 90\%$

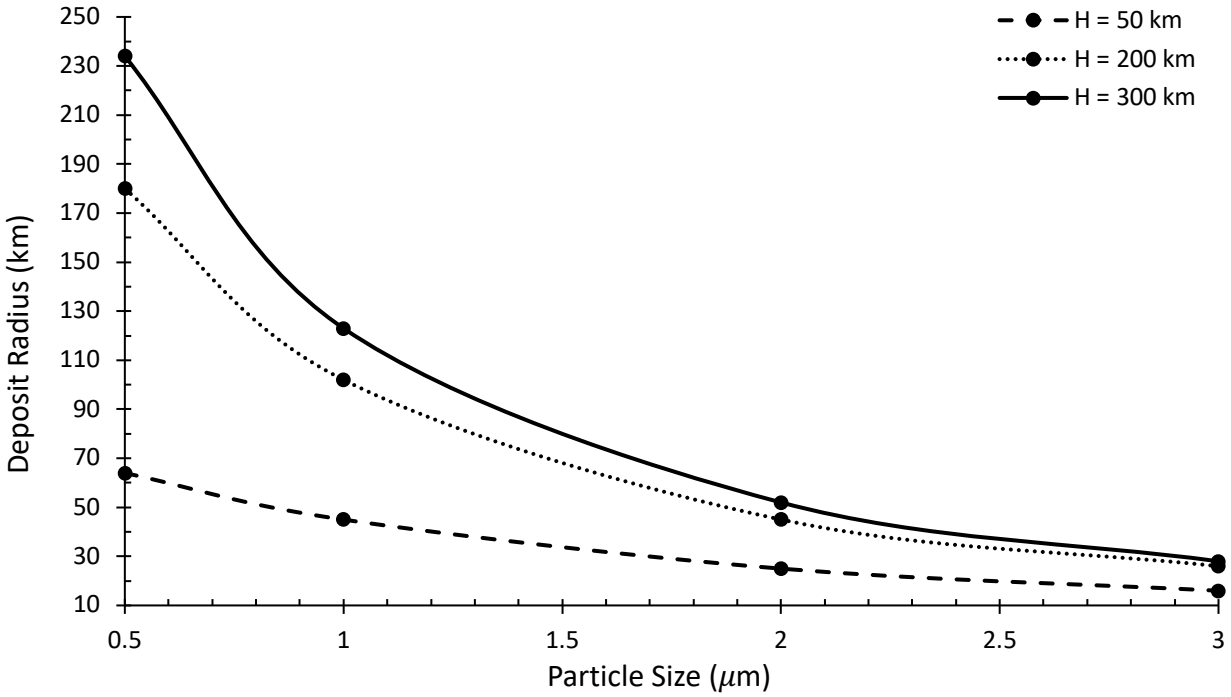

Figure 1. Maximum distance beyond the vent that icy particles reach, as a function of particle size, for plumes that are 50 km [*Sparks et al.*, 2017] and 200 km [*Roth et al.*, 2014] tall. We also plot maximum particle range for 300 km tall plumes, which may represent the largest possible plume observed on Europa according to *Roth et al.* [2014]. Each black dot, from the top left to the lower right of each data series, represents the particle sizes considered in this analysis: $r_p = 0.5$ μm, 1 μm, 2 μm, and 3 μm.

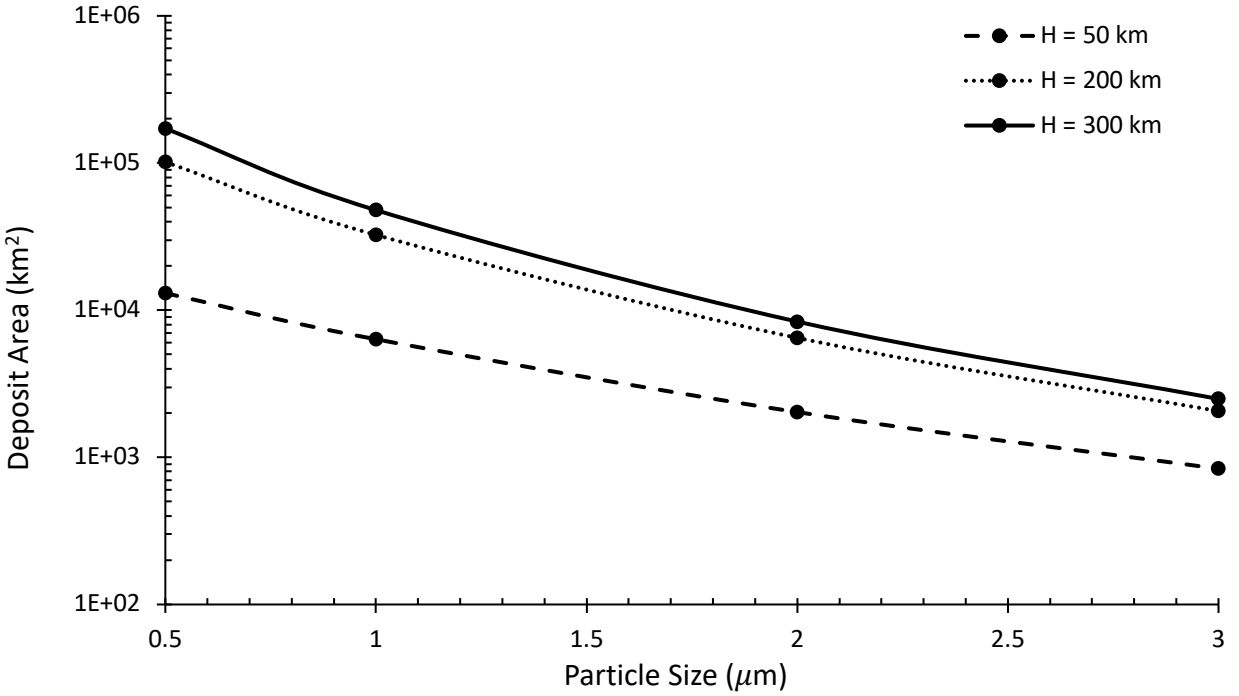

Figure 2. Areal extent of plume deposits as a function of primary particle size for plumes that are 50 km [*Sparks et al.*, 2017], 200 km, and 300 km tall [*Roth et al.*, 2014]. Each black dot, from the top left, to the lower right of each data series, represents the particle sizes considered in this analysis: r_p = 0.5 μm, 1 μm, 2 μm, and 3 μm.

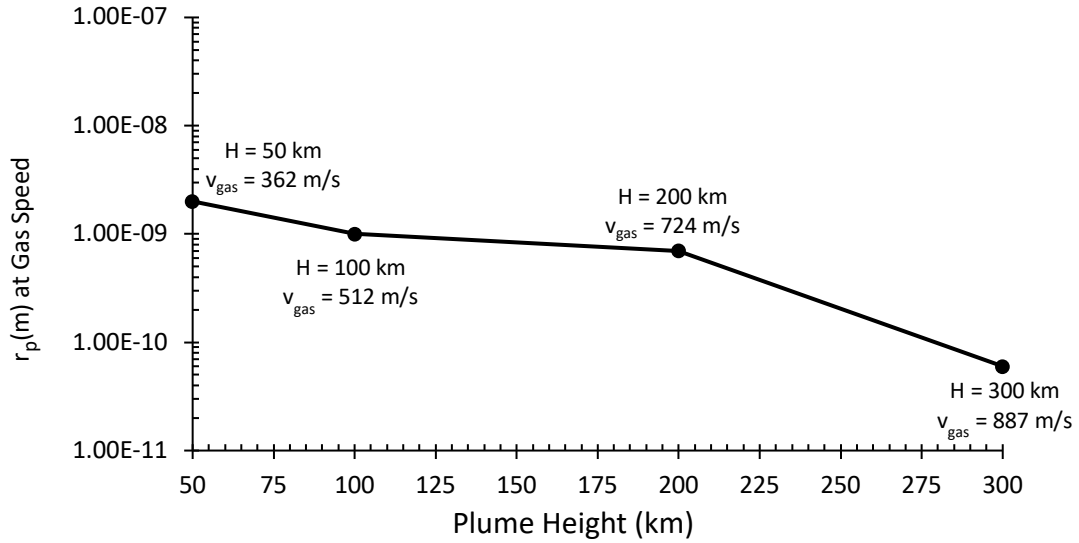

Figure 3. Size of particles that attain the gas speed as a function of plume height. The larger the plume, and the higher the gas velocity, the smaller constituent particles must be to remain entrained with the gas. For plume heights greater than 100 km, particle radii must be ~ $\leq 10^{-10}$ m to attain the gas speed.

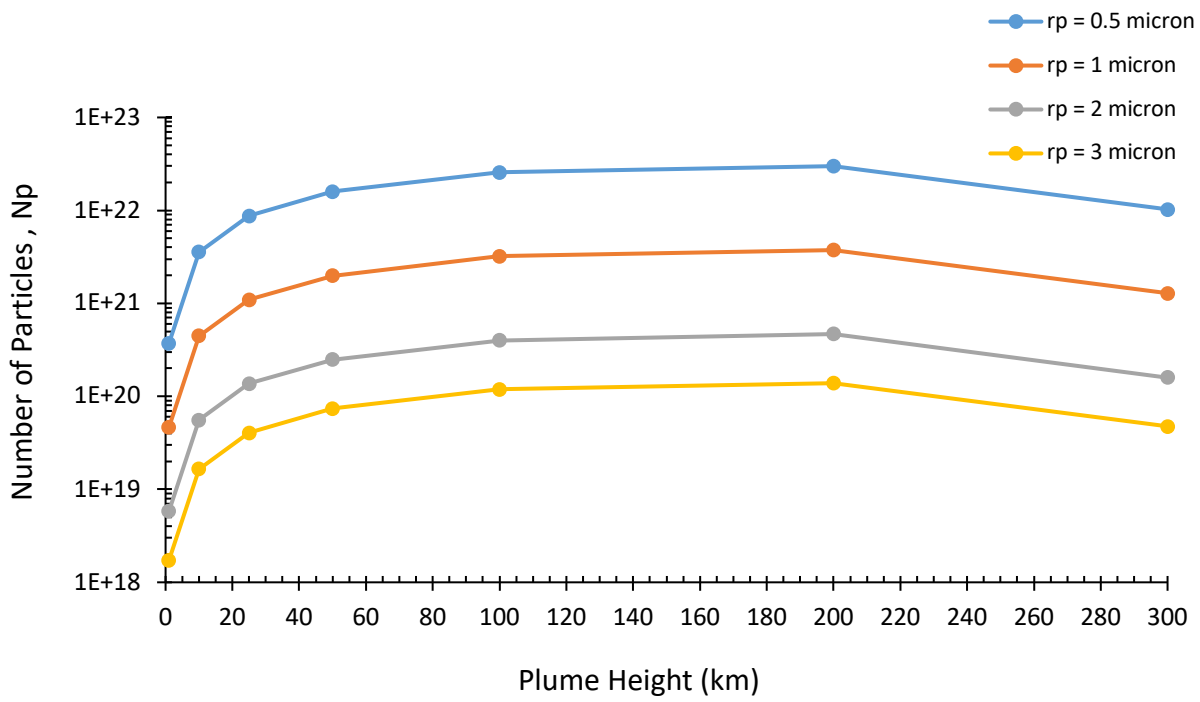

551

552 **Figure 4.** Particle population as a function of plume height. Regardless of plume height, the
553 number of particles in the smallest particle population in the plume (r_p = 0.5 μm) is larger than the
554 number of particles in the biggest particle population in the plume (r_p = 3 μm) by 2-3 orders of
555 magnitude.
556

557

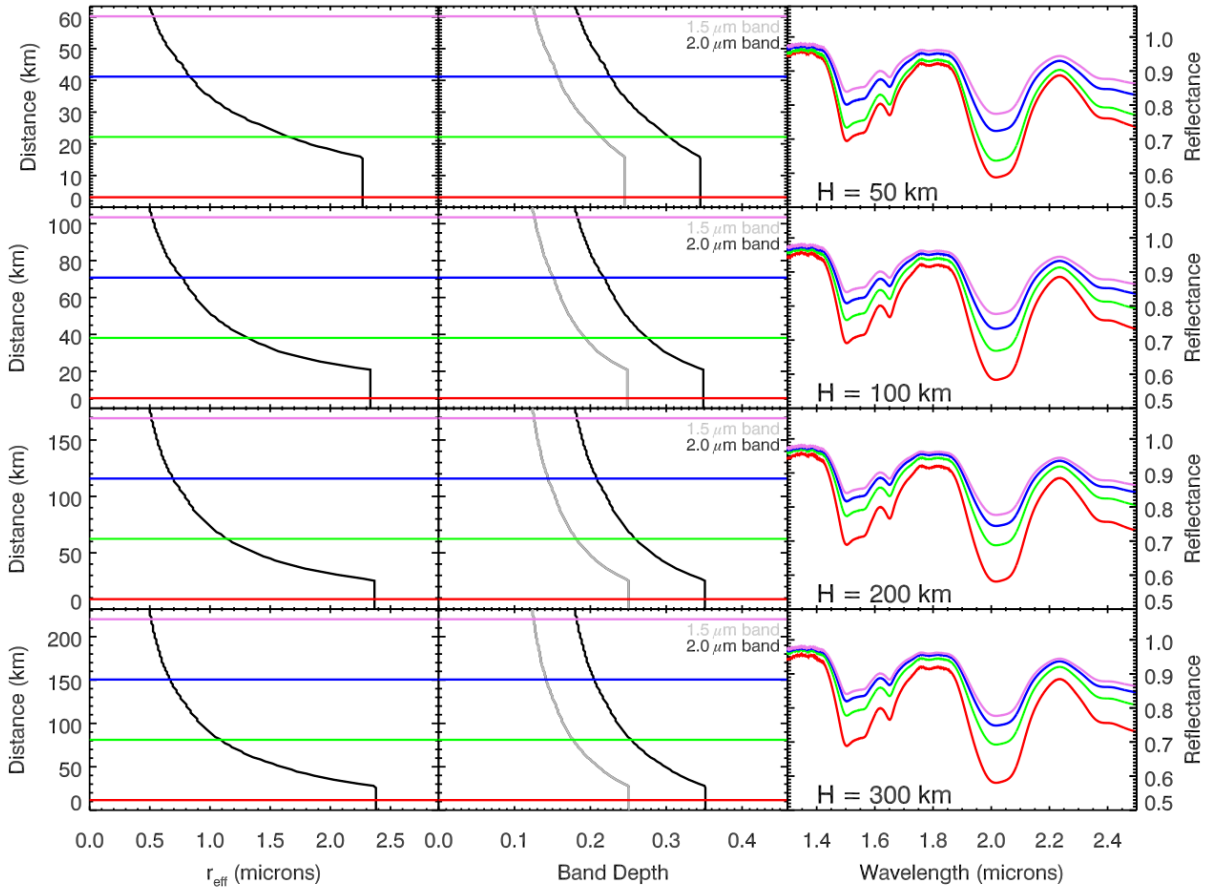

Figure 5. Average effective particle size and model spectra for deposits associated with a 50-300 km tall plumes. The left panels show average particle size as a function of distance from the vent, while the middle panel shows the expected depths of the water-ice bands as a function of distance from the vent. The right panel shows representative spectra at the distances marked with horizontal lines in the previous panels. Note that while the scale of the plumes changes, the overall trends in spectral properties are remarkably similar.

3.2 Spectral Model Results

Figure 5 illustrates how the average effective particle size and model surface spectra vary with distance from the vent for plumes with heights greater than 50 km (for shorter plumes, the uniform particle velocity leads to deposits with uniform spectral properties). The left panels show the effective average particle size versus distance from the vent. The middle panels show how the depths of the 1.5 and 2.0 μm water ice bands vary with distance from the vent, and the right panels

show representative spectra between 1.3 and 2.5 μm at a few selected distances from the vent. Recall that all these plots assume that the deposit is at least a few tens of microns thick, so that the underlying terrain does not contribute to the spectra.

For all of the simulated plumes, the effective particle size decreases with distance from the vent, which gives rise to a corresponding reduction in the depths of the water ice bands. This basic result simply reflects the fact that smaller particles are launched at higher speeds and so reach larger distances from the vent. Indeed, the observed trends are very similar for all the plume deposits shown in Figure 5. However, it is worth noting that the detailed shape of these trends is different for each plume. In particular, for the smaller plumes, the effective average particle size and band depths are constant over a larger fraction of the deposit because the particles are all launched at nearly the same speed (cf. Table 4a). For taller plumes, there are more substantial variations in the deposit's effective average particle size and band depths with distance from the vent. In addition, the maximum effective average particle sizes and band depths near the vent are slightly larger than they are for more compact plumes. This happens because the dispersion of launch velocities is higher, so the larger particles are now more concentrated near the vent.

4. Discussion

While the above simulations of plume particle dynamics and deposit spectra are rather idealized, estimates of the deposits' dimensions and their spectral trends are sufficient to identify the most promising observable signatures of recent activity on Europa. Below, we will consider the morphological indicators of plume deposits, and show that these are most likely to be detectable for very compact plumes whose resulting deposits accumulate rather quickly, and for plumes that are approximately 50 km tall, which are comprised of significantly more mass than plumes that are 10-25 km tall, and contain substantially more ice than the other large plumes we have

596 considered. Next, we consider the spectral signatures of emplaced deposits and show that these
597 may be a more promising approach for identifying fallout from larger and/or more transient
598 plumes.

599 **4.1 Morphological Signatures of Plume Deposits**

600 Europa was last imaged by the Galileo spacecraft in 2002 [*Alexander et al.*, 2009], and the
601 Europa Clipper spacecraft will reach the icy moon in the 2020s [*Phillips and Pappalardo*, 2014].
602 Assuming: (1) an approximately 25-year gap between the two missions, (2) that steady plume
603 eruptions occur on approximately hour-long timescales [*Sparks et al.*, 2017], and (3) that deposits
604 recognizable by cameras operating at visible wavelengths must be 1-10 m thick [*Quick et al.*,
605 2013], it is clear that deposits emplaced by very compact plumes will be easiest to identify on
606 Europa (Table 4a-c). For example, with particle deposition rates near 9×10^{-9} m/s , a 1 km tall
607 plume could emplace a ~ 7 m thick deposit with 50% porosity, or a 34 m thick deposit with 90%
608 porosity, if it erupted regularly, in the time between the two missions. Deposits emplaced by 1 km
609 tall plumes would therefore be relatively thick and should be easily identifiable by high-resolution
610 cameras, regardless of porosity. In general, we find that depending on deposit porosity, plumes
611 that are less than 7 km tall would emplace deposits that could grow to be tens of meters thick in
612 the time between the Galileo and Europa Clipper Missions. For example, applying the
613 methodology outlined in Section 2.1, we find that an 800 m tall plume could emplace a 42 m thick
614 deposit, assuming that the deposit has 90% pore space.

615 Conversely, our analysis shows that deposits emplaced by plumes that are ~10-25 km tall
616 could be somewhat difficult for spacecraft cameras to detect. Owing to the relatively low mass of
617 icy particles in these plumes (Table 3), and the large area over which deposits would be spread on
618 the surface, deposition rates for these intermediate-sized plumes would be quite low, making it

619 difficult for their deposits to accumulate sufficient mass in the time between the two missions to
620 be detected. Even if detectable deposits were emplaced on the surface, they may be rendered
621 unidentifiable by spacecraft cameras once they begin to coalesce and compress. For example, it
622 would take between 38 and 98 years for compact deposits emplaced by plumes that are 10-25 km
623 tall to grow to be 1 m thick (Table 4a). Further, although 10 km tall plumes could emplace ~ 3 m
624 thick deposits in the time between the two missions, particles would only be able to form a layer
625 this thick if the fraction of pore space between the particles remained very high. It is unknown
626 whether icy particles in Europa's surface environment could resist compression for the 25 years
627 between the two missions. As will be discussed in the next section, fresh surface deposits may be
628 degraded by processes such as sintering and micrometeorite bombardment within a matter of
629 decades [*Cooper et al.,*2001; *Tiscareno and Geissler,* 2003; *Carlson et al.* 2003; 2009].
630 In the case of plumes that are 50-300 km tall, we find that deposits would only accumulate
631 enough mass to be detected by cameras operating at visible wavelengths for a very specific set of
632 circumstances. Unless primarily composed of large particles, compact deposits (i.e., 50% pore
633 space) produced by 50-200 km tall plumes would fail to reach 1m thickness in the time between
634 the two missions. For example, deposits with 50% pore space that are emplaced by 50 km tall
635 plumes may accumulate to ~ 2-4 m thick if primarily composed of particles that are 2-3μm in
636 radius (Table 4b). Additionally, the 10^{-9}-10^{-8} m/s particle deposition rate for 50 km tall plumes
637 would allow deposits with 90% pore space to be detectable to spacecraft cameras, regardless of
638 the size of the constituent particles (Table 4b). Moreover, highly porous deposits that are primarily
639 composed of larger particles could grow to be as much as 23 meters thick in the time between the
640 two missions if emplaced by 50 km tall plumes (Table 4b). With the exception of plumes that are
641 on the order of 1 km tall, deposits emplaced by 50 km plumes would have the highest probability

642 of being detected by spacecraft cameras when compared to other large plumes (Table 4b). Indeed,
643 even deposits that are primarily composed of particles with 0.5μm radii would accumulate enough
644 mass to be detectable to visible imagers, provided that the deposits have a high percentage of pore
645 space. This is not the case for plumes that are ≥100 km tall. Tables 4b-c show that high-porosity
646 deposits emplaced by 100-300 km tall plumes would only be detectable if primarily composed of
647 particles that are ≥ 1μm in radius, and that deposits emplaced by these plumes may only grow to
648 be 10 m thick in the time between the two missions if they are composed of particles that are ≥
649 3μm in radius.

650 If deposits must indeed be 1-10 m thick to be visible to spacecraft cameras, we find that
651 that low-porosity deposits emplaced by 300 km tall plumes would not be detected by spacecraft
652 cameras operating at visible wavelengths at all. Compact deposits emplaced by 300 km tall plumes
653 would grow to be, at most, 10^{-3} mm thick in the intervening time between the Galileo and Europa
654 Clipper missions. If these deposits consist of large particles, they would take at least 27 years to
655 reach 1 m; if they primarily consist of small particles (e.g., 0.5 μm radii) it would take over 1800
656 years for them to emplace a 1 m thick layer on the surface (Fig. 4c). However, eruption of a 300
657 km tall plume could emplace a 1.4-5 m thick veneer of icy particles on Europa's surface if the
658 deposit is highly porous, and is primarily composed of particles that are ≥ 2μm in radius (Table
659 4c).

660 Owing to their high ice to vapor ratios, and their small area of particle fallout, our
661 calculations suggest that deposits emplaced by relatively small plumes, i.e., plumes that are < 7
662 km tall, would accumulate orders of magnitude faster and would be much thicker than their
663 counterparts that are emplaced by larger plumes. Based on the likely morphology of deposits
664 emplaced by large plumes, our analyses also suggest that it would be difficult for cameras

665 operating at visible wavelengths to identify surface deposits that have been emplaced by plumes
666 that are > 100 km tall unless the deposits are fresh, have been able to resist compression (i.e.,
667 remain highly porous), and/or are primarily composed of large particles. Features on Europa's
668 surface brighten with age, and young features appear dark due to their larger grain sizes [*Geissler*
669 *et al.*, 1998]. Hence assuming that they could accumulate enough mass, fresh deposits emplaced
670 by large plumes might be identifiable as anomalous patches of dark deposits against an otherwise
671 bright surface. Nevertheless, because these particles would be launched on trajectories that would
672 carry them so far across the surface (Table 4b-c), it could be difficult to trace the resulting deposits
673 back to their source locations. Further, as previously mentioned, any subsequent coalescence of
674 deposits emplaced by large plumes could render them undetectable.

675 For all plume sizes considered, we find that deposits with 90% pore space accumulate 5
676 times faster and are therefore on average, 5 times thicker than their more compact counterparts
677 that have only 50% pore space (Table 4). Accordingly, fresh, high-porosity deposits, and deposits
678 that primarily consist of larger particles (i.e., r_p = 2-3 μm) have the highest likelihood of being
679 detected by spacecraft cameras, regardless of the size of the plumes that emplace them. This could
680 suggest that if large plumes are common on Europa, and if these plumes leave behind surface
681 deposits that are thick enough to be identified by spacecraft cameras, that their average particle
682 sizes are at least on the order of 1μm, or that timescales for sintering or other processes that may
683 facilitate their compression, are relatively long. Conversely, large plumes on Europa might consist
684 of two particle populations, one which is composed of small particles that are entrained in the
685 water vapor and may only be visible at wavelengths shorter than visible (e.g., UV), and another
686 consisting of much larger particles that cluster near the vent. Enceladus' plumes are known to
687 include particles with a range of sizes, with larger particles being more likely to be deposited on

688 the moon's surface, while the smaller ones are more likely to escape into the E ring [*Porco et al.*,
689 2006; *Kempf et al.*, 2008; 2010; *Postberg et al.*, 2008; *Hedman et al.*, 2009; *Ingersoll and Ewald*,
690 2011]. The plume resulting from Io's Loki Patera also has two particle populations. Dust in the
691 "outer plume" is 10^{-3}-0.01 μm in radius and travels entrained in the SO_2 gas, and the dust in the
692 "inner plume" is 1-1000 μm in radius, decouples from the gas, and clusters close to the vent
693 [*Collins et al.*, 1981].

694 If Europan plumes consist of particle populations that are larger in size than those we
695 considered, this will have an effect on our reported ice to vapor ratios. Ice to vapor ratios for the
696 plumes we considered range from I/V = 0.1 for 300 km tall plumes to I/V = 332 for 1 km tall
697 plumes (Table 3). Although the ice to vapor ratios for plumes that are likely to leave behind the
698 most detectable deposits (H < 10 km) are much greater than the I/V estimated for plumes on
699 Enceladus, they are commensurate with ice to vapor ratios for modeled eruptions on Europa and
700 the Moon [*Wilson and Head*, 1983; *Fagents et al.*, 2000; *Quick et al.*, 2013]. In addition, ice to
701 vapor ratios for 50 to 100 km tall Europan plumes are the same order of magnitude as dust to gas
702 ratios for Io's Pele-type plumes and dust to gas ratios within the fine-grained dust component of
703 Prometheus-type plumes (e.g., Thor and Loki) where the dust to gas ratio = 1 [*Geissler and*
704 *McMillan*, 2008]. Further, ice to vapor ratios for 200-300 km tall plumes on Europa are within the
705 range of plausible ice to vapor ratios reported for plumes on Enceladus [*Porco et al.*, 2006; *Kieffer*
706 *et al.*, 2009; *Portyankina et al.*, 2017]. Moreover, Europa's plumes may differ significantly from
707 Enceladus' in a variety of ways, including in intensity, output, and periodicity [*Rhoden et al.*,
708 2015]. It is therefore possible that Europa's plumes also differ from Enceladus' in terms of particle
709 content. Bearing these details in mind, the ice to vapor ratios reported in Section 3, including the
710 high ice to vapor ratios reported for small europan plumes, seem plausible.

We note however, that our analysis has assumed an idealized case where at least the smallest plume particles issue from the vent at velocities that are equal to the gas velocity. In reality, icy particles will issue from the vent at velocities that are somewhat slower than the gas, resulting in a low I/V at the foot of a plume. Additionally, as the gas and icy particles will reach different scale heights, I/V in the upper portions of plumes will be different from I/V at other locations. Moreover, observers may report a line-of-sight integrated I/V. For all of these reasons, the values of n_{gas}, n_f, M_v, M, and I/V listed for each plume in Table 3 may be substantially different from what is directly observed. This could also be the reason for the order of magnitude difference between the total water vapor mass calculated for the 200 km plume in Section 2 (Table 3), and the value reported (i.e., 1.46 x 10^6 kg) in *Roth et al.* [2014]. Additionally, we have scaled total plume mass according to plume height, using water vapor column densities reported in *Sparks et al.* [2017] as a baseline. However, preliminary calculations using the methods described in Section 2 suggest that if the total mass of water vapor in all of Europa's plumes, regardless of their size, is on the order of 10^6 kg, deposits that are composed of pure water ice and are emplaced by plumes ≥100 km tall, would not be easily detected. We note that although *Roth et al.* [2014] observed plumes that were 200 ± 100 km tall, and *Sparks et al.* [2016; 2017] reported repeat observations of a 50 km tall plume, both of these authors reported total water vapor masses of ~10^6 kg in the plumes they observed. This could indicate the total plume mass does not scale with plume height, or that the actual column densities of Europa's plumes differ from what is inferred from observation.

Observational Constraints: Rhadamanthys and Androgeous Linea

Previous workers have suggested that lineaments could be sites of recent geological activity on Europa [*Geissler et al.*, 1998]. Indeed, *Fagents et al.* [2000] and *Quick et al.* [2013]

734 considered that the low-albedo deposits which flank Rhadamanthys Linea (Fig. 11) and
735 Androgeous Linea (Fig. 12) may be mantlings of cryoclastic particles that were emplaced by
736 plumes. Rhadamanthys was imaged at 230 m/pixel and 1.6 km/pix during Galileo's E15 and G1
737 orbits, respectively, and Androgeous was imaged at 20 m/pix during Galileo's E6 orbit of Europa.
738 The highest resolution images of Rhadamanthys, taken during Galileo's E15 orbit, provide the
739 most accurate measurements of the dimensions of its low-albedo flanking deposits. The average
740 radii of deposits flanking Rhadamanthys range from ~ 2 to 7 km, while the broadest portion of the
741 deposit flanking Androgeous is approximately 3 km wide [*Fagents et al.*, 2000, Tables I & III].
742 Based on the visibility of preexisting topographic features beneath these deposits in Galileo
743 imagery, and on Europa's 10^{-6} m/yr surface erosion rate [*Cooper et al.*, 2001], *Quick et al.* [2013]
744 estimated these deposits to be 1-10 m thick. According to Table 4a, above, and Tables IIIa-IIIb of
745 *Fagents et al.* [2000], the dimensions of these deposits are consistent with emplacement by plumes
746 that were < 10 km tall.
747 Pre-existing topographic features are clearly visible beneath the low-albedo material
748 flanking Rhadamanthys (Fig. 11). It is therefore reasonable to assume that the Rhadamanthys
749 deposits are on the order of 1 m thick. According to Table 4a, the smallest Rhadamanthys deposits,
750 i.e., those that are approximately 2 km in radius, could have been emplaced by 1 km tall plumes.
751 Assuming 50% deposit porosity, we could expect each eruption to emplace a veneer of plume
752 material with a maximum thickness of 0.12 mm. At these deposition rates, ~ 8333 eruptions would
753 have to occur in order for a 1m thick deposit to accumulate. Assuming a deposit with 90% porosity,
754 each eruption would emplace a veneer of plume material with a maximum thickness of 0.62 mm
755 so that an approximately 1m thick veneer would accumulate after ~ 1613 eruptions. We find that
756 it takes ~ 3.7 years for a 1 m thick deposit with 50% porosity to form, and ~ 9 months for a 1 m

757 thick deposit with 90% porosity to form. In both cases, it would take a minimum of 6 eruptions
758 per day to emplace just one of the smallest deposits in Fig. 11. At present, it is not clear if Europa's
759 plumes are tidally modulated (e.g., see *Rhoden et al.* [2015]). Hence in all of these cases, the
760 amount of time required to accumulate the modeled cryoclastic deposits is reported as a function
761 of Earth days.

762 The largest Rhadamanthys deposit is ~ 7 km in radius [*Fagents et al.*, 2000]. Calculations
763 using the procedures outlined in Section 2.1 suggest that its dimensions are consistent with having
764 been emplaced by plumes that are 3.5 km tall. A 3.5 km tall plume could emplace a 0.04 mm thick
765 deposit with 50% porosity each time it erupts. In this case, 25,000 eruptions would be required for
766 a 1m thick deposit to form. We find that compact, 1m thick deposits emplaced by 3.5 km tall
767 plumes would take approximately 13 years to accumulate. This suggests that 1923 eruptions per
768 year, or 5 eruptions per day would be required to form the widest Rhadamanthys-flanking deposit
769 (profile R18 in Table I of *Fagents et al* [2000]). Conversely, if the resulting deposit has 90% pore
770 space, a 0.18 mm thick veneer would be emplaced on the surface after each eruption, and ~ 5556
771 eruptions would had to have occurred in order to for a 1m thick deposit to form. Calculations
772 using the methods introduced in Section 2 suggest that 1m thick deposits could form in 2.6 years.
773 This again suggests that over 2000 eruptions per year, or ~ 6 eruptions/day, would have been
774 necessary to produce these deposits. Thus, regardless of porosity and the size of the resulting
775 deposits, we find that a minimum of 5-6 eruptions per day would have been required to produce
776 the Rhadamanthys deposits.

777 The deposits flanking Androgeous Linea (Fig. 12) appear to obscure more of the
778 background plains than those that lie along Rhadamanthys. Because Androgeous was imaged at a
779 much higher resolution than Rhadamanthys [*Fagents et al.*, 2000], it is possible that this

780 heightened obscuration of the background plains is apparent rather than actual. Nevertheless,
781 because of the decreased visibility of Androgeous' preexisting topographic features relative to
782 Rhadamanthys' (Fig. 11), it appears that the dark deposits that flank the former are somewhat
783 thicker than those flanking the latter. It is therefore possible that the low-albedo deposits lying
784 along Androgeous Linea are ~10 m thick. Assuming plume eruptions took place at the edge of
785 Androgeous, as noted in *Fagents et al.* [2000], we find that the 3 km wide portion of the
786 Androgeous deposit could have been emplaced by plumes that were on the order of 0.8 km tall. If
787 these deposits have 50% pore space, each eruption would emplace a veneer of material with a
788 maximum thickness of approximately 0.16 mm, and ~ 63,000 eruptions would have to occur before
789 a 10 m thick deposit could accumulate. We find that these eruptions would occur over, at most, 28
790 years' time, indicating that at a minimum, 186 eruptions per month, or just over 6 eruptions per
791 day, would be required to form the broadest portion of the Androgeous deposit. Assuming deposits
792 with 90% porosity, each eruption would emplace a veneer of plume material with a maximum
793 thickness of 0.8 mm so that a 10 m thick veneer would accumulate after ~ 12,500 eruptions. In this
794 instance, approximately 5.6 years would elapse before a 10 m thick deposit would accumulate on
795 the surface. This equates to a minimum of 2232 eruptions per year, or once again, just over 6
796 eruptions per day, in order for these deposits to accumulate.
797

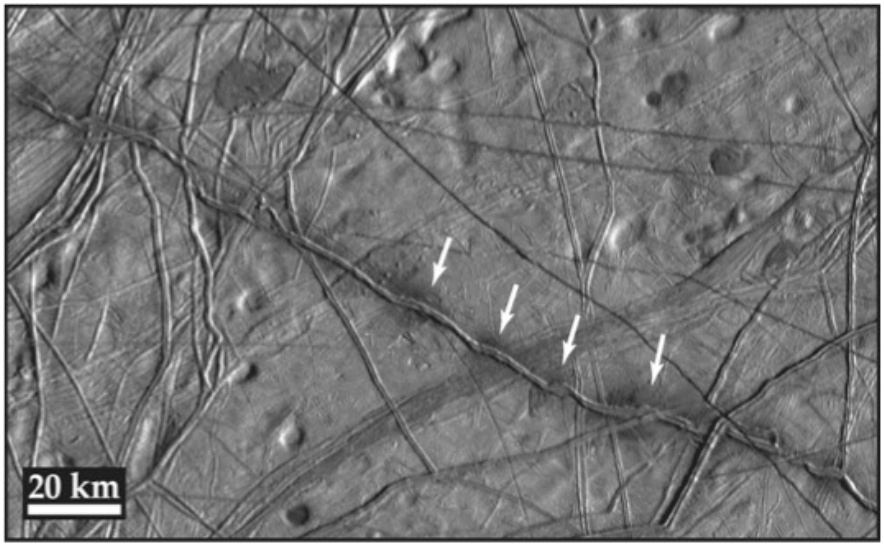

Figure 11. Rhadamanthys Linea from the Galileo spacecraft's E15 orbit of Europa at 230 m/pixel. The low-albedo deposits flanking this feature are indicated by the white arrows. These deposits range from approximately 2 – 7 km in radius (4 – 14 km in width) and may be cryoclastic mantlings that were emplaced by plumes.

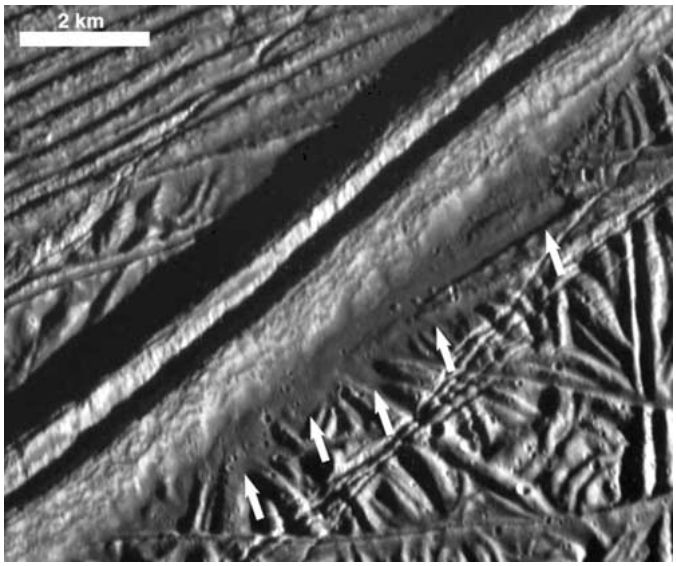

Figure 12. Segment of the prominent double ridge, Androgeous Linea. Image taken during Galileo's E6 orbit of Europa at 20 m/pixel. White arrows point to flanking low-albedo deposits that may be cryoclastic mantlings. According to *Fagents et al.* [2000], the broadest portion of this deposit is approximately 3 km wide.

4.2 Spectral and Photometric Signatures of Plume Deposits

While significant accumulation is needed to produce observable morphological signatures of plume deposits, spectral signatures can arise with much thinner deposits. In general,

electromagnetic radiation only penetrates to depths a few times larger than the observed wavelength. Thus, a deposit that is only 10-100 μm thick would be enough to substantially affect the spectral properties of the surface at visible and near-infrared wavelengths. Even the 200-km tall plume considered above would produce a deposit of order 10 μm thick over the course of only a few days, so in principle even very short-lived eruptions could produce surface deposits with detectable trends in their spectral properties. These spectral signatures also extend over large regions and so do not require high spatial resolutions to detect, making them a promising way to search for deposits from large and/or intermittent plumes. Indeed, the spectral models discussed in Section 3.2 show that even if the plume particles do not have a distinctive composition, that the deposits can exhibit detectable spectral signatures. For example, the band depths of even a pure ice deposit from a 200-km high plume vary by a factor of two across a deposit hundreds of kilometers wide (see Figure 10). Detecting such a trend with a suitable near-infrared spectrometer would therefore only require spatial resolutions of order 10 km. More compact deposits would require correspondingly higher resolution, but the spectral variations associated with even a 10-km tall plume would still only require spatial resolutions on the order of 1 km.

Of course, in reality both the average size and the composition of plume particles can vary with distance from the vent, which could give rise to trends in wide variety of spectral and photometric parameters. For example, Europan plume deposits may contain significant fractions of non-ice material, perhaps in the form of condensed CO_2, SO_2, etc. [*Fagents et al.*, 2000], and the low-albedo deposits along Rhadamanthys and Androgeous may contain a significant fraction of salt species [*McCord et al.*, 1998; 1999; *Shirley et al.*, 2010]. Indeed, previous workers have suggested that low-albedo deposits on Europa's surface are likely composed of salts and other contaminants originating from the subsurface ocean or other internal liquid reservoirs [*Shirley et*

836 *al*., 2010; *Prockter et al.*, 2017]. If this is the case for the lineae-flanking deposits considered here,
837 this would imply that the low-albedo spots along Rhadamanthys and Androgeous lineae are
838 photometrically dark due to their composition. The density of NaCl is approximately equal to 2200
839 kg/m^3. Independent calculations using equations (2)-(5) with ρ_p = 2200 kg/m^3 suggest that plumes
840 $\geq$ 50 km tall could emplace deposits with radii on the order of 5-6 km, consistent with the
841 dimensions of the largest Rhadamanthys deposits (see Table IIIa of *Fagents et al.*, 2000), if the
842 erupted particles are primarily composed of salt, and are rather large, with average radii equal to
843 3μm. Eruptions of a 200 km tall plume could emplace a 15 μm thick deposit, with 50% pore
844 space, composed primarily of 3μm salt particles, in about 7.5 years. A similar deposit with 90%
845 pore space could form in just 1.5 years. Similar to the case for the emplacement of ice-dominated
846 deposits, if the small Rhadamanthys deposits and the deposits flanking Androgeous Linea are
847 primarily composed of salts, they were likely to have been emplaced by plumes < 4 km tall.

848 One potential challenge to identifying spectral and photometric signatures of plume
849 deposits is that spectral signatures could be more transient than morphological signatures. Europa's
850 surface spectra vary on a wide range of scales, with darker regions generally showing larger
851 concentrations of non-icy materials (see *Carlson et al.,* 2009, and references therein). While some
852 of these variations could be due to Europa's geological history and activity, others are almost
853 certainly due to the surface being modified by the radiation environment. Radiation exposure can
854 sinter grains, implant molecules, and sputter ice, while micrometeorites can mix surface deposits
855 with underlying material. Various calculations indicate that these processes will mix or
856 contaminate freshly exposed surfaces to depths of order 10-100 μm on timescales of order decades
857 [*Cooper et al.,*2001; *Tiscareno and Geissler,* 2003; *Carlson et al.* 2003; 2009]. Hence the spectral
858 and photometric signatures of surface deposits may become undetectable if they are more than a

few decades old. Fortunately, the presence of dark patches around Rhadamanthys Linea, and the fact that dark terrains along lineae correspond to regions with higher fractions of non-ice material [*McCord et al.*, 1998; 1999], suggest that compact patches are emplaced regularly enough to maintain their distinct spectral and photometric properties. Alternatively, these deposits could have distinct compositional or structural features that are not easily erased by radiation exposure. If the former is correct, then this would imply that deposits from small plumes will likely be easier to detect both spectroscopically and morphologically. On the other hand, if the deposits have a persistent compositional signature, larger deposits could be easier to detect because they require lower resolution data. The possibility that 200 km tall plumes could emplace substantial deposits in the time between the Galileo and Europa Clipper missions, suggests that it is possible for plumes with ice to vapor ratios equal to 0.67 (Table 3), which is approximately equal to the maximum end of the *I*/*V* range *Ingersoll and Ewald* [2011] considered for plumes on Enceladus, to produce recognizable deposits on Europa's surface. For all other cases, the ice to vapor ratios of plumes that are likely to have produced the deposits are larger by several orders of magnitude.

5. Conclusions

In the absence of direct detection of plumes, plume deposits would provide the best evidence of recent geological activity on Europa and could also serve as important indicators for where to search for ongoing activity. We find that plumes that are less than 7 km tall are most likely to emplace deposits that are thick enough to be detected by spacecraft cameras operating at visible wavelengths. Mantlings emplaced by these plumes could accumulate to form deposits that are 1 - 10 m thick in as little as 7 months' time. If eruptive activity has occurred frequently on Europa since the Galileo Mission, these deposits could be substantial today, perhaps on the order of tens of meters thick. Moreover, we find that at most, ~ 5 - 6 eruptions/day of plumes that are

882 0.8-3.5 km tall are enough to produce the candidate cryoclastic mantlings flanking lineaments on
883 Europa. Deposits emplaced by large plumes will be spread over large areas of the surface, but may
884 accumulate enough mass to be detected by cameras operating at visible wavelengths if they are
885 composed of particles > 0.5μm. Larger particles would cluster close to the source vent and the
886 resulting deposits would be identifiable by cameras operating at visible wavelengths. Regardless
887 of the size of the plumes that emplace them, we find that fresh, highly porous cryoclastic deposits
888 and deposits that are primarily composed of particles with radii $\geq$ 2μm would be most visible from
889 the point of view of spacecraft imagers, and hence most easily detected. Our analyses also indicate
890 that any deposits that may have been emplaced by 100-300 km plumes would be visible to
891 spacecraft cameras, provided that they are highly porous and/or composed of large particles.
892 Nevertheless, within the parameter space explored here, we find that deposits emplaced plumes
893 that are < 7 km tall, would be the easiest to detect.

894 Large candidate plumes that may be sporadic in nature have recently been observed on
895 Europa. If these plumes are outliers, and most plumes on Europa are small in stature as suggested
896 by previous modeling and image analysis, strategies for plume detection on the ocean moon should
897 not only consider the potential periodicity of Europa's eruptions, but they should also consider the
898 possibility that a significant number of Europa's plumes may be compact. Comprehensive plume
899 search strategies should therefore include high-resolution imaging of low-albedo deposits that may
900 have been emplaced via eruptive venting. These searches should pay special attention to the
901 deposits that flank lineated features such as Rhadamanthys and Androgeous Lineae, and
902 subsequent analyses should be carried out to determine if the albedos and/or dimensions of these
903 deposits have changed in the time since the Galileo spacecraft first visited Europa.

The Europa Clipper spacecraft could constrain the amount of activity occurring along lineaments by acquiring high-resolution imagery of Androgeous and Rhadamanthys Linea. If the deposits that flank these features were indeed emplaced by plumes, then three scenarios are possible: (1) If Europa Clipper finds that the deposits have brightened and/or appear shrunken, then that would suggest that plume activity along these features ceased in the intervening decades between the two missions; (2) If imagery from Europa Clipper reveals that the albedo and dimensions of these deposits have remained unchanged since Galileo, then eruptions may have occurred along these lineaments in the time between the two missions, albeit at a steady state that allowed for the overall abundance of particles deposited onto the surface to remain constant; (3) If the deposits appear darker and wider in Europa Clipper imagery, then this might indicate that plume activity not only occurred continuously in the time between the two missions, but that plume output rates increased in the intervening years. This could take the form of material erupting from relatively small plumes for long periods of time between the two missions, or, could suggest that additional material was emplaced sporadically by large plumes in the intervening decades.

The Europa Imaging System (EIS) on Europa Clipper is well-suited to test the findings reported here and will be able to place improved constraints on the constitution of plume deposits. EIS will be able to detect surface color changes caused by the deposition of micron-sized plume particles, and stereo imaging by the Narrow Angle Camera (NAC) will be ideal for constraining the thicknesses of candidate plume deposits that flank lineaments and any other features [*Turtle et al.*, 2016; 2019]. Moreover, deposits emplaced by small plumes should be easily detected by EIS during its local- and regional-scale imaging campaigns. As previously mentioned, even if Europa Clipper does not directly detect plumes on Europa, their presence could be indirectly inferred via

comparison of the dimensions of low-albedo deposits as they appear in Galileo imagery, with their appearance in high-resolution imagery acquired by EIS.

Meanwhile, the Mapping Imaging Spectrometer for Europa (MISE) will obtain near-infrared spectra of Europa's surface between 0.8 and 5.0 μm at 10 nm spectral resolution, and at spatial resolutions better than 10 kilometers on global scales, 500 meters at regional scales, and 25 meters at local scales [*Blaney et al.*, 2019]. This investigation will therefore be able to detect variations in both the surface composition and typical regolith particle sizes on scales comparable to many of the plume deposits considered here. Therefore, MISE will also place reasonable constraints on the levels of Europa's recent plume activity, particularly for large plumes whose morphological signatures may be difficult to discern.

Acknowledgements

This work was supported in part by NASA through the Europa Clipper Project. We thank Sarah Fagents and an anonymous reviewer for feedback that improved the quality of this manuscript. We also thank Lionel Wilson for helpful discussions.

References

Alexander, C., Carlson, R., Consolmagno, G., Greeley, R., Morrison, D., 2009. The Exploration History of Europa. In: Pappalardo, R.T., McKinnon, W. B. and Khurana, K. (Eds.), Europa. University of Arizona Press, Tucson, pp. 3-26.

Batista, E. R., Ayotte, P., Bilic, A., Kay, B. D., Jonsson, H., 2005. What Determines the Sticking Probability of Water Molecules on Ice? Physical Review Letters 95, 223201.

Berg, J. J., Goldstein, D. B., Varghese, P. L., Trafton, L. M., 2016. DSMC Simulation of Europa Water Vapor Plumes. Icarus 277, 370-380.

D.L. Blaney, C. Hibbitts, R.O. Green, R.N. Clark, J.B. Dalton, A.G. Davies, Y. Langevin, J.I. Lunine, M.M. Hedman, T.B. McCord, S.L. Murchie, C. Paranicas, F.P. Seelos, J.M. Soderblom, S. Diniega, M. Cable, D. Thompson, C. Bruce, A. Santo, R. Redick, D. Hahn, H. Benderm, B. Van Gorp, J. Rodriguez, P. Sullivan, T. Nevillem S. Lundeen, M. Bowers, K. Ryan, J. Hayes, B. Bryce, R. Hourani, E. Zarate, L.B. Moore, K. Maynard, I.M. McKinley, D. Johnson, P. Aubuchon, J. Fedosi, R. Wehbe, R. Calvet, P. Mouroulis, V. White, D. Wilson. 2019. The Europa Clipper Mapping Imaging Spectrometer for Europa

(MISE): Using Compositional Mapping to Understand Europa. 50th Lunar and Planetary Science Conference, Abstract #2132.
Bramson, A. M., Phillips, C. B., Emery, J. C., 2011. A Search for Geologic Activity on Jupiter's Satellites. 42nd Lunar and Planetary Science Conference, Abstract #1606.
Carlson, R.W., Calvin, W. M., Dalton, J.B., Hansen, G. B., Hudson, R.L., Johnson, R. E., McCord, T. B., Moore, M. H., 2009. Europa's Surface Composition. In: Pappalardo, R. T., McKinnon, W. B. and Khurana, K. (Eds.),Europa. University of Arizona Press, Tucson, pp. 283-327.
Carlson, R.W, Anderson, M. S., Johnson, R. E., Schulman, M. B., A.H. Yavrouian, A. H., 2002. Sulfuric Acid production on Europa: The Radiolysis of Sulfur in Water Ice. Icarus, 157, 456-463.
Collins, S. A., 1981. Spatial Color Variations in the Volcanic Plume at Loki, on Io. Journal of Geophysical Research 86, 8621-8626.
Cook, A.F., Danielson, G.E., Jewitt, D.C., Owen, T., 1981.Dust Observations in the Jovian System. Advances in Space Research 1, COSPAR, Great Britain, 99–101.
Cooper, J.F., Johnson, R. E., Mauk, B. H., Garrett, H.B., Gehrels, N., 2001. Energetic Ion and Electron Irradiation of the Icy Galilean Satellites. Icarus 149, 133-159.
Crawford, G. D., Stevenson, D. J., 1988. Gas-Driven Water Volcanism and the Resurfacing of Europa. Icarus 73, 66-79.
Cuffey, K.M., Paterson, W. S. B., 2010. The Physics of Glaciers, Fourth Edition, Elsevier, USA.
Cuzzi, J. N., Estrada, P. R., 1998. Compositional Evolution of Saturn's Rings Due to Meteoroid Bombardment. Icarus 132, 1–35.
Degruyter, W., Manga, M., 2011. Cryoclastic Origin of Particles on the Surface of Enceladus. Geophysical Research Letters 38, L16201.
Europa Study Team, 2012. Europa Study 2012 Report. Task Order NMO11062, NASA/Jet Propulsion Laboratory.
Fagents, S.A., Greeley, R., Sullivan, R.J., Pappalardo, R.T., Prockter, L.M., 2000. Cryomagmatic Mechanisms for the Formation of Rhadamanthys Linea, Triple Band Margins, and Other Low Albedo Features on Europa. Icarus 144, 54-88.
Fagents, S. A., 2003. Considerations for Effusive Cryovolcanism on Europa: The Post-Galileo Perspective. Journal of Geophysical Research 108, 5139.
Gaidos, E. J., Nimmo, F., 2000. Tectonics and Water on Europa. Nature 405, 637.
Johnson, T. V., Matson, D. L., Blaney, D. L., Veeder, G. J., 1995. Stealth Plumes on Io. Geophysical Research Letters 22, 3293-3296.
Geissler, P.E., Greenberg, R., Hoppa, G., McEwen, A., Tufts, R., Phillips, C., Clark, B., Ockert-Bell, M., Helfenstein, P., Burns, J., Veverka, J., Sullivan, R., Greeley, R., Pappalardo, R.T., Head, J.W., Belton, M.J.S., Denk, T., 1998. Evolution of Lineaments of Europa: Clues from Galileo Multispectral Imaging Observations. Icarus 135, 107-126.
Geissler, P., McEwen, A., Phillips, C., Keszthelyi, L., Spencer, J., 2004. Surface Changes on Io During the Galileo Mission. Icarus 169, 29-64.
Geissler, P. E., Goldstein, D. B., 2006; Plumes and their Deposits. In: Lopes, R. M. C., and Spencer, J. R. (Eds.), Io After Galileo: A New View of Jupiter's Volcanic Moon. Springer Praxis Books, New York, NY, pp. 163-192.
Geissler, P. E., McMillan, M. T., 2008. Galileo Observations of Volcanic Plumes on Io. Icarus 197, 505-518.
Glaze, L. S., Baloga, S. M., 2000. Stochastic-Ballistic Eruption Plumes on Io. Journal of

1003 Geophysical Research 105, 17579-17588.
1004 Hapke, B. 1981. Bidirectional Reflectance Spectroscopy. I - Theory. Journal of Geophysical
1005 Research 86, 3039–3054.
1006 Hapke, B. 1993. Theory of Reflectance and Emittance Spectroscopy. Cambridge University Press,
1007 Cambridge, UK.
1008 Hedman, M. M., Nicholson, P. D., Showalter, M. R., Brown, R. H., Buratti, B. J., Clark, R. N.,
1009 2009. Spectral Observations of the Enceladus Plume with Cassini-VIMS. The
1010 Astrophysical Journal 693,1749–1762.
1011 Hedman, M.M., Nicholson, P. D., Cuzzi, J. N., Clark, R. N., Filacchione, G., Capaccioni, F.,
1012 Ciarniello, M., 2013. Connections Between Spectra and Structure in Saturn's Main Rings
1013 Based on Cassini VIMS Data. Icarus 223, 105-130.
1014 Hedman, M. M., Dhingra, D., Nicholson, P. D., Hansen, C. J., Portyankina, G., Ye, S., Dong, Y.,
1015 2018. Spatial Variations in the Dust-to-Gas Ratio of Enceladus' Plume. Icarus 305, 123-
1016 138.
1017 Hsu, H.-W., Postberg, F., Sekine, Y., Shibuya, T., Kempf, S., Horányi, M., Juhász, A., Altobelli,
1018 N., Suzuki, K., Masaki, Y., Kuwatani, T., Tachibana, S., Sirono, S.-i., Moragas-
1019 Klostermeyer, G., Srama, R., 2015. Ongoing Hydrothermal Activities within Enceladus.
1020 Nature 519, 207-210.
1021 Ingersoll, A. P., Ewald, S. P., 2011. Total Particulate Mass in Enceladus Plumes and Mass of
1022 Saturn′s E ring Inferred from Cassini ISS Images. Icarus 216, 492–506.
1023 Jia, X., Kivelson, M. G., Khurana, K. K., Kurth, W. S., 2018. Evidence of a Plume on Europa from
1024 Galileo Magnetic and Plasma Wave Signatures. Nature Astronomy 2, 459-464.
1025 Kempf, S., Beckmann, U., Moragas-Klostermeyer, G., Postberg, F., Srama, R., Economou, T.,
1026 Schmidt, J., Spahn, F., Grun, E., 2008. The E-ring in the Vicinity of Enceladus: I. Spatial
1027 Distribution and Properties of Ring Particles. Icarus 193,420–437.
1028 Kempf, S., Beckmann, U., Schmidt, J., 2010. How the Enceladus Dust Plume Feeds Saturn's E
1029 Ring. Icarus 206, 446-457.
1030 Kieffer, S.W., Lu, X., McFarquhar, G., Wohletz, K.H., 2009. A Redetermination of the Ice/Vapor
1031 Ratio of Enceladus′ Plumes: Implications for Sublimation and the Lack of a Liquid Water
1032 Reservoir. Icarus 203, 238–241.
1033 Mahieux, A., Goldstein, D. B., Varghese, P. L., Trafton, L. M., 2019. Parametric Study of Water
1034 Vapor and Water Ice Particle Plumes Based on DSMC Calculations: Application to the
1035 Enceladus Geysers. Icarus 319, 729-744.
1036 Mastrapa, R. M., Sandford, S. A., Roush, T. L., Cruikshank, D. P., Ore, C.M.D., 2009. Optical
1037 Constants of Amorphous and Crystalline H_2O-ice: 2.5-22 μ m (4000-455 cm^{-1}) Optical
1038 Constants of H_2O-ice. The Astrophysical Journal 701, 1347-1356.
1039 McCord, T.B., Hansen, G. B., Fanale, F.P., Carlson, R.W., Matson, D. L., Johnson, T. V., Smythe,
1040 W. D., Crowley, J. K., Martin, P. D., Ocampo, A., Hibbitts, C.A., Granahan, J. C., 1998.
1041 Salts on Europa's Surface Detected by Galileo's Near-Infrared Mapping Spectrometer.
1042 Science 280, 1242.
1043 McCord, T.B., Hansen, G. B., Matson, D. L., Johnson, T. V., Crowley, J. K., Fanale, F. P.,
1044 Carlson, R.W., Smythe, E.D., Martin, P.D., Hibbitts, C. A., Granahan, J. C., Ocampo, A.
1045 Hydrated Salt Minerals on Europa's Surface from the Galileo Near-Infrared Mapping
1046 Spectrometer (NIMS) investigation. Journal of Geophysical Research 104, 11827-11852.
1047 Nordheim, T. A., Hand, K. P., Paranicas, C., 2018. Preservation of Potential Biosignatures in the
1048 Shallow Subsurface of Europa. Nature Astronomy 2 673-679.

1049 Pappalardo, R., Senske, D., Prockter, L., Paczkowski, B., Vance, S., Rhoden, A., Goldstein, B.,
1050 Magner, T., Cooke, P., 2015. Science Objectives for the Europa Clipper Mission Concept:
1051 Investigating the Potential Habitability of Europa. European Planetary Science Conference
1052 10, Abstract #EPSC2015-156.
1053 Parfitt, E. A., Wilson, L., 2008. Fundamentals of Physical Volcanology. Blackwell Publishing,
1054 Malden, MA.
1055 Phillips, C. B., McEwen, A.S., Hoppa, G.V., Fagents, S.A., Greeley, R., Klemaszewski, J.E.,
1056 Pappalardo, R.T., Klaasen, K.P., Breneman, H.H., 2000. The Search for Current Geologic
1057 Activity on Europa. Journal of Geophysical Research 105, 22579-22597.
1058 Phillips, C. B., Pappalardo, R. T., 2014. Europa Clipper Mission Concept: Exploring Jupiter's
1059 Ocean Moon. Eos 95, 165-167.
1060 Porco, C.C., Helfenstein, P., Thomas, P. C., Ingersoll, A.P., Wisdom, J., West, R., Neukum, G.,
1061 Denk, T., Wagner, R., Roatsch, T., Kieffer, S., Turtle, E., McEwen, A., Johnson, T.V.,
1062 Rathbun, J., Veverka, J., Wilson, D., Perry, J., Spitale, J., Brahic, A., Burns, J.A.,
1063 DelGenio, A.D., Dones, L., Murray, C.D., Squyres, S., 2006. Cassini Observes the Active
1064 South Pole of Enceladus. Science 311,1393–1401.
1065 Porco, C. C., Dones, L., Mitchell, C., 2017. Could it Be Snowing Microbes on Enceladus?
1066 Assessing Conditions in its Plume and Implications for Future Missions. Astrobiology 17,
1067 876-901.
1068 Portyankina, G., Hedman, M. M., Hansen, C. J., Esposito, L. W., Aye, K. -M., Dhingra, D., 2017.
1069 Simultaneous Cassini UVIS and VIMS Solar Occultation Observations: Modeling Insights.
1070 48th Lunar and Planetary Science Conference. Abstract #2418.
1071 Postberg, F., Kempf, S., Hillier, J.K., Srama, R., Green, S.F., McBride, N., Grun, E., 2008. The E-
1072 Ring in the Vicinity of Enceladus: II. Probing the Moon′s Interior - The Composition of E-
1073 Ring Particles. Icarus 193, pp.438–454.
1074 Postberg, F., Schmidt, J., Hillier, J., Kempf, S., Srama, R., 2011. A Salt-Water Reservoir as the
1075 Source of a Compositionally Stratified Plume on Enceladus. Nature 474, 620-622.
1076 Postberg, F., Khawaja, N., Abel, B., Choblet, G., Glein, C. R., Gudipati, M., Henderson, B. L.,
1077 Hsu, H.-.W., Kempf, S., Klenner, F., Moragas-Klostermeyer, G., Magee, B., Nölle, L.,
1078 Perry, M., Reviol, R., Schmidt, J., Srama, R., Stolz, F., Tobie, G., Trieloff, M., Waite, J.
1079 H., 2018. Macromolecular Organic Compounds from the Depths of Enceladus. Nature 558,
1080 564-567.
1081 Poulet, F., Cuzzi, J. N., Cruikshank, D. P., Roush, T., Dalle Ore, C.M, 2002. Comparison Between
1082 the Shkuratov and Hapke Scattering Theories for Solid Planetary Surfaces: Application to
1083 the Surface Composition of Two Centaurs. Icarus 160, 313–324.
1084 Prockter, L. M., Shirley, J. H., Dalton, J. B. III, Kamp, L., 2017. Surface Composition of Pull-
1085 Apart Bands in Argadnel Regio, Europa: Evidence of Localized Cryovolcanic Resurfacing
1086 During Basin Formation. Icarus 285, 27-42.
1087 Quick, L. C., Barnouin, O. S., Prockter, L. M., Patterson, W. G., 2010. Constraints on the Detection
1088 of Cryovolcanic Plumes on Europa. 41st Lunar and Planetary Science Conference, Abstract
1089 #2247.
1090 Quick, L. C., Barnouin, O. S., Prockter, L. M., Patterson, W. G., 2013. Constraints on the
1091 Detection of Cryovolcanic Plumes on Europa. Planetary and Space Science 86, 1-9.
1092 Rathbun, J., Spencer, J., 2018. A Closer Look at Galileo Thermal Data from Possible Plume
1093 Sources Near Pwyll, Europa. 50th Meeting of the AAS Division for Planetary
1094 Sciences, Abstract #403.06

1095 Rathbun, J., Spencer, J., 2019. Proposed Plume Source Regions on Europa: No Evidence for
1096 Endogenic Thermal Emission. Icarus, In Press.
1097 Rhoden, A. R., Hurford, T. A., Roth, L., Retherford, K., 2015. Linking Europa's Plume Activity
1098 to Tides, Tectonics, and Liquid Water. Icarus 253, 169-178.
1099 Roth, L., Saur, J., Retherford, K.D., Strobel, D.F., Feldman, P.D., McGrath, M.A., Nimmo, F.,
1100 2014. Transient Water Vapor at Europa's South Pole. Science 343, 171-174.
1101 Schmidt, J., Brilliantov, N., Spahn, F., Kempf, S., 2008. Slow Dust in Enceladus′ Plume from
1102 Condensation and Wall Collisions in Tiger Stripe Fractures. Nature 451, 685–688.
1103 Schmidt, B. E., Blankenship, D. D., Patterson, G. W., Schenk, P. M., 2011. Active Formation
1104 of Chaos Terrain Over Shallow Subsurface Water on Europa. Nature 479, 502-505.
1105 Shaw, R. A., Lamb, D., 1999. Experimental Determination of the Thermal Accommodation
1106 and Condensation Coefficients of Water. Journal of Chemical Physics 111, 10659-10663.
1107 Shirley, J. H., Dalton, J. B. III, Prockter, L. M., Kamp, L. W., 2010. Europa's Rigid Plains and
1108 Smooth Low Albedo Plains: Distinctive Compositions and Compositional Gradients at the
1109 Leading Side-Trailing Side Boundary. Icarus 210, 358-384.
1110 Shkuratov, Y., Starukhina, L, Hoffmann, H., Arnold, G., 1999. A Model of Spectral Albedo of
1111 Particulate Surfaces: Implications for Optical Properties of the Moon. Icarus 137, 235–
1112 246.
1113 Spahn, F., Schmidt, J., Albers, N., Horning, M., Makuch, M., Seib, M., Kempf, S., Srama, R.,
1114 Dikarev, V., Helfert, S., Moragas-Klostermeyer, G., Krivov, A.V., Sremcevic, M.,
1115 Tuzzolino, A.J., Economou, E., Grun, E., 2006. Cassini Dust Measurements at Enceladus
1116 and Implications for the Origin of the E Ring. Science 311, 1416–1418.
1117 Southworth, B. S., Kempf, S., Schmidt, J., 2015. Modeling Europa's Dust Plumes. Geophysical
1118 Research Letters 42, 10451-10458.
1119 Sparks, W. B., Hand, K. P., McGrath, M. A., Bergeron, E., Cracraft, M., Deustua, S. E., 2016.
1120 Probing for Evidence of Plumes on Europa with HST/STIS. The Astrophysical Journal
1121 829, 121.
1122 Sparks, W. B., Schmidt, B. E., McGrath, M. A., Hand, K. P., Spencer, J. R., Cracraft, M., Deustua,
1123 S. E., 2017. Active Cryovolcanism on Europa? The Astrophysical Journal Letters 839, L18.
1124 Strom, R.G., Schneider, N.M., Terrile, R.J., Cook, A. F., Hansen, C., 1981.Volcanic Eruptions on
1125 Io. Journal of Geophysical Research 86, 8593–8620.
1126 Tiscareno, M.S., Geissler, P. E., 2003. Can Redistribution of Material by Sputtering Explain the
1127 Hemispheric Dichotomy of Europa? Icarus 161, 90-101.
1128 Turtle, E.P., McEwen, A.S., Barr, A. C., Collins, G.C., Fletcher, L. N., Hansen, C, J., Hayes, A.,
1129 Hurford, T.A., Kirk, R.L., Nimmo, F., Patterson, G.W., Quick, L.C., Soderblom, J.M.,
1130 Thomas, N., Ernst, C., 2016. The Europa Imaging System (EIS): High-Resolution Imaging
1131 and Topography to Investigate Europa's Geology, Ice Shell, and Potential for Current
1132 Activity. 47th Lunar and Planetary Science Conference, Abstract #1626.
1133 Turtle, E. P., McEwen, A. S., Collins, G. C., Dauber, I. J., Ernst, C. M., Fletcher, L., Hansen, C.
1134 J., Hawkins, S. E., Hayes, A. G., Humm, D., Hurford, T. A., Kirk, R. L., Kutsop, N., Barr
1135 Mlinar, A. C., Nimmo, F., Patterson, G. W., Phillips, C. B., Pommerol, A., Prockter, L.,
1136 Quick, L. C., Reynolds, E. L., Slack, K. A., Soderblom, J. M., Sutton, S., Thomas, N.,
1137 Bland, M., 2019. The Europa Imaging System (EIS): High-Resolution, 3-D Insight into
1138 Europa's Geology, Ice Shell, and Potential for Current Activity. 50th Lunar and Planetary
1139 Science Conference, Abstract #3065.
1140 Wilson, L., Head, J. W. III, 1983. A Comparison of Volcanic Eruption Processes on Earth, Mars,

Moon, Io, and Venus. Nature 302, 663-669.
Ye, S.-Y., Gurnett, D.A., Kurth, W.S., Averkamp, T.F., Kempf, S., Hsu, H.-W., Srama, R., Grun, E., 2014. Properties of Dust Particles near Saturn Inferred from Voltage Pulses Induced by Dust Impacts on Cassini Spacecraft. Journal of Geophysical Research: Space Physics 119, 6294-6312.
Yeoh, S. K., Chapman, T. A., Goldstein, D. B., Varghese, P. L., Trafton, L. A., 2015. On Understanding the Physics of Enceladus South Polar Plume Via Numerical Simulation. Icarus 253, 205-222.
Zhang, J., Goldstein, D. B., Varghese, P. L., Trafton, L., Moore, C., Miki, K., 2004. Numerical Modeling of Ionian Volcanic Plumes with Entrained Particulates. Icarus 172, 479-502.